nature metabolism

ARTICLES

https://doi.org/10.1038/s42255-020-00330-2

Check for updates

NADPH levels affect cellular epigenetic state by inhibiting HDAC3–Ncor complex

Wei Li[1,4], Junjie Kou[1,4], Junying Qin[2,4], Li Li[1], Zhenxi Zhang[1], Ying Pan[3], Yi Xue[3]✉ and Wenjing Du[1]✉

NADPH has long been recognized as a key cofactor for antioxidant defence and reductive biosynthesis. Here we report a metabolism-independent function of NADPH in modulating epigenetic status and transcription. We find that the reduction of cellular NADPH levels, achieved by silencing malic enzyme or glucose-6-phosphate dehydrogenase, impairs global histone acetylation and transcription in both adipocytes and tumour cells. These effects can be reversed by supplementation with exogenous NADPH or by inhibition of histone deacetylase 3 (HDAC3). Mechanistically, NADPH directly interacts with HDAC3 and interrupts the association between HDAC3 and its co-activator nuclear receptor corepressor 2 (Ncor2; SMRT) or Ncor1, thereby impairing HDAC3 activation. Interestingly, NADPH and the inositol tetraphosphate molecule Ins(1,4,5,6)P_4 appear to bind to the same domains on HDAC3, with NADPH having a higher affinity towards HDAC3 than Ins(1,4,5,6)P_4. Thus, while Ins(1,4,5,6)P_4 promotes formation of the HDAC3–Ncor complex, NADPH inhibits it. Collectively, our findings uncover a previously unidentified and metabolism-independent role of NADPH in controlling epigenetic change and gene expression by acting as an endogenous inhibitor of HDAC3.

NADPH is a key component in cellular anti-oxidation systems and an indispensable electron donor in numerous enzymatic reactions and biosynthetic reactions, such as nucleotide synthesis, lipid synthesis and chain elongation of fatty acids[1]. NADPH scarcity is believed to be a limiting step for cell proliferation[2]. For instance, reducing NADPH production by suppression of the NADPH-generating pathway(s) leads to severe cell proliferation arrest, senescence or even apoptosis[3–6]. Generally, there are three major direct routes for NADPH production: glucose-6-phosphate dehydrogenase (G6PD) in the oxidative pentose phosphate pathway (oxPPP), methylenetetrahydrofolate dehydrogenase (MTHFD) in folate metabolism and malic enzymes (MEs) in glutaminolysis[4,6]. Of note, MEs act as a predominant source of cellular NADPH in adipocytes[7]. Besides the long-recognized involvement of NADPH in reductive biosynthetic reactions and redox control, an understanding of the physiological function of NADPH remains almost stagnant for decades. Moreover, many tumour cells exhibit altered fluxes of NADPH-generating pathways and elevated NADPH production to support their rapid proliferation[3,4,6,8]. However, how tumour cells sense cellular NADPH change and what advantages it can afford to tumour cells are largely unknown.

In eukaryotic cells, histone acetylation and methylation are strongly associated with chromatin accessibility and gene transcription. Methylation is correlated either with permissive (tri-methylation of histone H3 Lys4) or with repressive transcription (tri-methylation of histone H3 Lys9 or Lys27). By contrast, histone acetylation loosens the chromatin structure, rendering DNA more accessible to transcription factors by creating docking sites for the binding of bromodomain-containing regulatory proteins and neutralizing the positive charge on histones to reduce the electrostatic attraction to the negatively charged DNA backbone. Histone acetylation is dynamically regulated by histone acetyltransferases (HATs) and deacetylases (HDACs), and these processes are nutrient responsive and involved in the regulation of various physiological events[9]. For instance, the metabolite acetyl coenzyme A (acetyl-CoA), whose levels are correlated with histone acetylation in both yeast and some types of tumour cells, stimulates HAT activities[10–14]. Moreover, NAD^+, a cofactor of sirtuins (SIRTs; class III HDACs), promotes histone deacetylation[12,15–18].

Unlike most other deacetylases, HDAC3 uniquely forms a complex with Ncor1 or the silencing mediator of retinoic and thyroid receptors Ncor2 (SMRT)[19,20]. Binding to the deacetylase activating domain (DAD) of Ncor is thought to be assembled by Ins(1,4,5,6)P_4 and causes HDAC3 conformational change, which is more accessible for its substrate and results in enhanced enzyme activity[21,22]. Here we found that the reducing equivalent NADPH acts as an endogenous inhibitor of HDAC3. Through directly interrupting the assembly of HDAC3 and SMRT-DAD, NADPH suppresses HDAC3 activity and reprograms histone acetylation and gene expression.

Results

Malic enzyme depletion impairs global histone acetylation. We previously found that MEs function in NADPH metabolism and senescence[6]. To further explore the precise effect of MEs, we knocked down *ME* expression in 3T3-L1 preadipocytes, which predominantly use MEs to produce NADPH[7]. As shown in Fig. 1a, 3T3-L1 preadipocytes transfected with *ME1*, *ME2* or control small interfering RNA (siRNA) were induced to differentiate into mature adipocytes using a standard differentiation protocol[23]. Interestingly, compared to control siRNA cells, *ME1*- or *ME2*-depleted cells had a noticeable reduction in the differentiation-induced lipid accumulation as shown by Oil Red O staining and lipid content quantification (Fig. 1a,b). This differentiation-inhibitory effect of *ME* silencing was also observed when two separate sets of siRNAs were

[1]State Key Laboratory of Medical Molecular Biology, Key Laboratory of RNA Regulation and Hematopoiesis, Department of Cell Biology, Institute of Basic Medical Sciences Chinese Academy of Medical Sciences, School of Basic Medicine Peking Union Medical College, Beijing, China. [2]School of Life Sciences, Tsinghua University, Beijing, China. [3]School of Life Sciences, Tsinghua-Peking Joint Center for Life Sciences; Beijing Advanced Innovation Center for Structural Biology, Tsinghua University, Beijing, China. [4]These authors contributed equally: Wei Li, Junjie Kou, Junying Qin. ✉e-mail: yixue@mail.tsinghua.edu.cn; wenjingdu@ibms.pumc.edu.cn

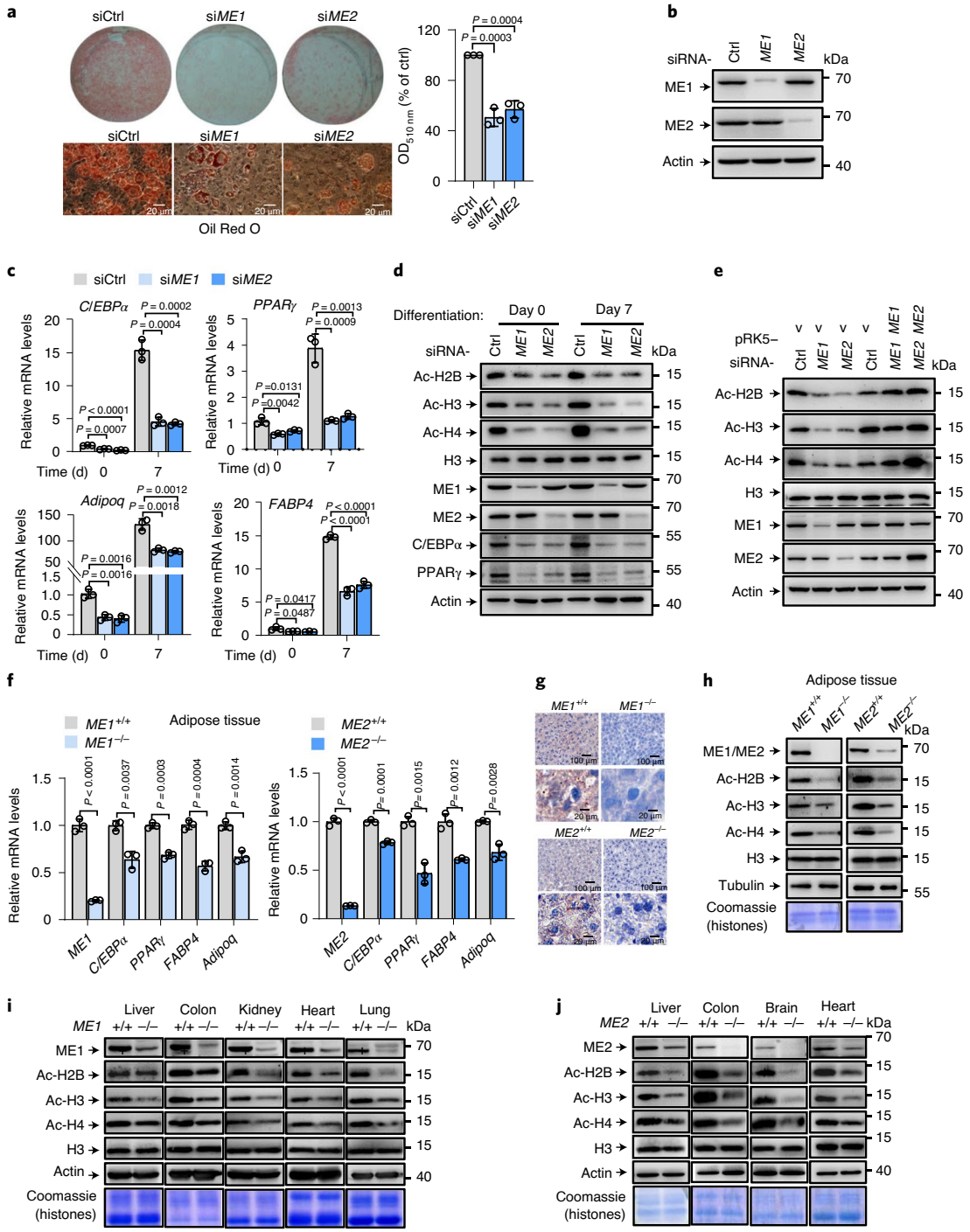

Fig. 1 | Malic enzyme silencing suppresses adipocytic gene transcription and global histone acetylation, resulting in a block to adipocyte differentiation. **a**,**b**, The 3T3-L1 preadipocytes were transfected with *ME1*, *ME2* or control siRNA (siCtrl) for 2 d, then stimulated to differentiate into adipocytes. After 7 d, cells were fixed and stained with Oil Red O. **a**, Wells and higher magnification images are shown (left). Oil Red O staining was quantified (right). OD, optical density. **b**, Protein expression is shown. **c**,**d**, The 3T3-L1 preadipocytes were transfected with control, or different sets of *ME1* or *ME2* siRNAs and induced to differentiate for 7 d. **c**, mRNA levels of adipocyte-specific genes and transcription factors. **d**, Effect of *ME* knockdown on acetylated histones expression, C/EBPα and PPARγ expression levels. **e**, The 3T3-L1 preadipocytes were transfected with control, *ME1* or *ME2* siRNA and stimulated to differentiate for 7 d in the presence or absence of exogenous *ME1* or *ME2* cDNA. Protein expression is shown. **f**, mRNA expression of *ME1*, *ME2* and adipocyte-specific genes from the adipose tissues of *ME1* or *ME2* knockout mice. **g**, Representative Oil Red O staining of liver microscopic appearance. **h**, Effect of *ME1* or *ME2* knockout on acetylated histone expression levels in mouse adipose tissue. **i**,**j**, Protein expression from several tissues of *ME1* (**i**) or *ME2* (**j**) knockout mice was detected using western blotting. Data in **a** are from $n=3$ biological replicates and **c** and **f** from $n=3$ technical replicates from one of three independent experiments with similar results. Data are the mean ± standard deviation (s.d.). Statistical significance was determined by two-tailed unpaired *t*-test. In **b**, **d**, **e** and **g**–**j**, Oil Red O staining images and western blots are representative of three independent experiments. For all western blot data, histone expression levels (Ac-H2, Ac-H3, Ac-H4 and total H3) were analysed using acid-extracted cell lysates; total H3 and/or Coomassie Brilliant Blue staining were used as loading controls. All other protein expression levels (ME1, ME2, C/EBPα and PPARγ) were assessed with total cell lysates; tubulin or actin was used as loading control. The samples were derived from the same experiment and the gels/blots were processed in parallel.

used (Extended Data Fig. 1a,b). Next, we examined the expressions of adipogenic genes that are critical for differentiation initiation. The siRNA-mediated silencing of *ME1* or *ME2* led to a significant decrease in mRNA levels of CCAAT/enhancer-binding protein alpha (*C/EBPα*) and peroxisome proliferator-activated receptor γ (*PPARγ*), two key transcription factors that are essential for executing adipogenesis, an adipocytic lineage-specific gene *Adipoq*[24] and the adipocytic marker fatty acid-binding protein 4 (*FABP4*; Fig. 1c). Similar effects were obtained with two more sets of siRNAs targeting different regions of *ME* mRNA under both undifferentiating and differentiating conditions (day 0 and day 7; Extended Data Fig. 1c,d). Consistently, the expressions of adipogenic genes also decreased in both un-induced (day 0) and differentiated (day 7) 3T3-L1 cells engineered with CRISPR–Cas9 to knock out *ME* (Extended Data Fig. 1e). Thus, these findings suggest that MEs play a role in modulating gene transcription.

We next explored the mechanism by which MEs regulate gene transcription. The transcriptional factor p53 suppresses adipocyte differentiation, and MEs restrain its activity[6,25]. To examine whether MEs regulate adipocytic gene transcription via p53, we knocked down *p53* in 3T3-L1 cells. After differentiation induction, *ME1*- or *ME2*- depleted cells still exhibited visibly fewer lipid droplets and reduced expression of *C/EBPα*, *PPARγ*, *Adipoq* and *FABP4* compared to their control siRNA counterparts, even in the absence of p53 (Extended Data Fig. 1f–h), suggesting that the effect of MEs on adipogenic gene expression is p53 independent.

Histone acetylation is associated with chromatin remodelling and gene transcription and increases substantially during 3T3-L1 preadipocyte differentiation[14,26]. We therefore sought to determine whether MEs modulate histone acetylation, thereby affect adipogenic gene expression. Correlating with gene expression findings (Fig. 1c and Extended Data Fig. 1c–e), silencing of *ME1* or *ME2* decreased the levels of total histone acetylation for all core histones examined in both un-induced cells (day 0) and cells in differentiation (day 7; Fig. 1d). Similar results were also obtained with two more sets of *ME* siRNAs in differentiating cells (Extended Data Fig. 1i). Consistently, cells expressing *ME1* or *ME2* single guide RNA (sgRNA) displayed reduced histone acetylation under both undifferentiating and differentiating conditions (Extended Data Fig. 1j). To further exclude the off-target effect of siRNA, we performed a rescue experiment using RNAi-resistant *ME1* and *ME2* cDNA. As shown in Fig. 1e, enforced expression of exogenous ME1 or ME2 rescued the expression of MEs, and also restored histone acetylation in *ME*-depleted cells. Next, we extended our studies into animals. In adipose tissue, expression levels of *C/EBPα*, *PPARγ*, *Adipoq* and *FABP4* were reduced in either *ME1* or *ME2* knockout mice compared to wild-type (WT) mice (Fig. 1f). Moreover, Oil Red O staining of liver tissue from *ME* knockout mice showed decreased lipid levels compared with those of controls (Fig. 1g). Notably, knockout of either *ME1* or *ME2* decreased histone acetylation substantially in mouse adipose tissue (Fig. 1h). Similar results were also observed in several other tissues (Fig. 1i,j). Thus, MEs regulate adipogenic gene expression independent of differentiation but correlating with histone acetylation. Previous studies indicate that the reduction in global histone acetylation alters the expression of multiple glucose metabolism genes[14,27]. These observations raised the possibility that the role of MEs in regulating histone acetylation may affect expression of genes involved in glucose utilization in highly proliferating cells such as tumour cells. Thus, we extended our studies to cancer cells by knocking down *ME* in human osteosarcoma U2OS cells. Indeed, silencing of *ME1* or *ME2* reduced histone acetylation and decreased expression of glucose metabolic genes, including glucose transporter 4 (*Glut4*, official gene symbol *SLC2A4*), glycolytic regulators hexokinase 2 (*HK2*), phosphofructokinase 1 (*PFK1*, official gene symbol *PFKM*), lactate dehydrogenase A (*LDHA*), glutamate oxaloacetate transaminase (*Got1*) and carbohydrate-response element-building protein (*ChREBP*, official gene symbol *MLXIPL*) (Extended Data Fig. 2a,b). Consistent with this, a relative reduction in glucose uptake and lactate production was observed in *ME*-depleted cells (Extended Data Fig. 2c). Together, these findings demonstrate that suppression of *ME* correlates with decreased histone acetylation and transcription.

HDAC3 mediates malic enzyme-regulated histone acetylation. Next, we investigated how MEs manipulate histone acetylation. Histone acetylation is dynamically regulated by HATs and HDACs, which are devoted to the addition and elimination of acetyl groups from lysine residues on the histone N-terminal tails, respectively. However, silencing of *ME1* or *ME2* failed to affect HAT activity, suggesting that *ME*-mediated histone acetylation is not dependent on HAT (Fig. 2a). Growing evidence suggests that deacetylation is a central switch for the transition from metabolic signals to gene transcription[14,15,18,28,29]. Thus, we investigated whether the decrease in histone acetylation induced by *ME* knockdown could be reversed by HDAC inactivation. Strikingly, addition of trichostatin A (TSA), a HDAC class I/II inhibitor[30,31], restored the levels of the lipid droplet accumulation in cells depleted of *ME1* or *ME2* (Extended Data Fig. 3a). In keeping with this, TSA supplementation augmented the expressions of *C/EBPα*, *PPARγ*, *Adipoq* and *FABP4* (Extended Data Fig. 3b). Moreover, TSA also reversed the decreased histone acetylation by *ME* depletion (Extended Data Fig. 3c). In contrast to TSA, treatment with nicotinamide (NAM), a SIRTs inhibitor, failed to affect ME-mediated histone acetylation (Extended Data Fig. 3d). Together, these findings indicate that ME-maintained histone acetylation is specific to HDAC classes I and II, and critical for 3T3-L1 cells to execute adipocyte differentiation.

We next sought to determine which HDAC(s) mediate(s) the effect of MEs on histone acetylation. Specifically, histone acetylation elevated in *ME*-depleted cells treated with HDAC1/3 inhibitor RG2833 (RGFP109)[32,33], but not HDAC6 inhibitor WT161 (ref. [34]), or LMK-235, an inhibitor of HDAC4 and HDAC5 (ref. [35]; Fig. 2b). These results suggest that HDAC1 or HDAC3 may play a role in *ME*-mediated histone acetylation.

Furthermore, by supplying cells with siRNAs individually targeting *HDACs 1–6*, we found that histone acetylation increased only when HDAC3 was knocked down in cells depleted of *ME* (Extended Data Fig. 3e). Interestingly, HDAC3 was found to be significantly activated when *ME1* or *ME2* was knocked down in 3T3-L1 cells (Fig. 2c). Consistent with this, HDAC3 activity increased in tissues including adipose tissue from *ME1* or *ME2* knockout mice (Fig. 2d,e). By assessing the effect of HDAC3 on *ME*-mediated histone acetylation, we found that *HDAC3* silencing significantly reversed histone acetylation defects in *ME*-depleted cells (Fig. 2f). To further confirm these findings, we used the HDAC3 inhibitor RGFP966 (ref. [36]). Consistently, pharmacological inhibition of HDAC3 rescued the levels of acetylation of histones in *ME1*- or *ME2*-depleted cells relative to control cells during differentiation (Extended Data Fig. 3f). Likewise, in human tumour cells, addition of RGFP966 increased overall histone acetylation in U2OS cells and colon cancer HCT116 cells, and minimized the differences in the levels of histone acetylation between control cells and *ME1*- or *ME2*-depleted cells (Extended Data Fig. 3g). Together, these findings indicate that *ME*-regulated histone acetylation is dependent on HDAC3 activity.

Next, we examined the role of HDAC3 in regulating adipocyte differentiation. The silencing of *HDAC3* significantly increased the adipogenic gene expression (Extended Data Fig. 3h). We then investigated whether blocking HDAC3-mediated erasure of histone acetylation is a required component of ME-regulated adipocyte differentiation. After differentiation induction, cells treated with *ME1* or *ME2* siRNA exhibited reduced ability to differentiate into adipocytes, whereas this effect could be reversed by *HDAC3* knockdown (Fig. 2g). Moreover, silencing of *ME1* or *ME2* led to a

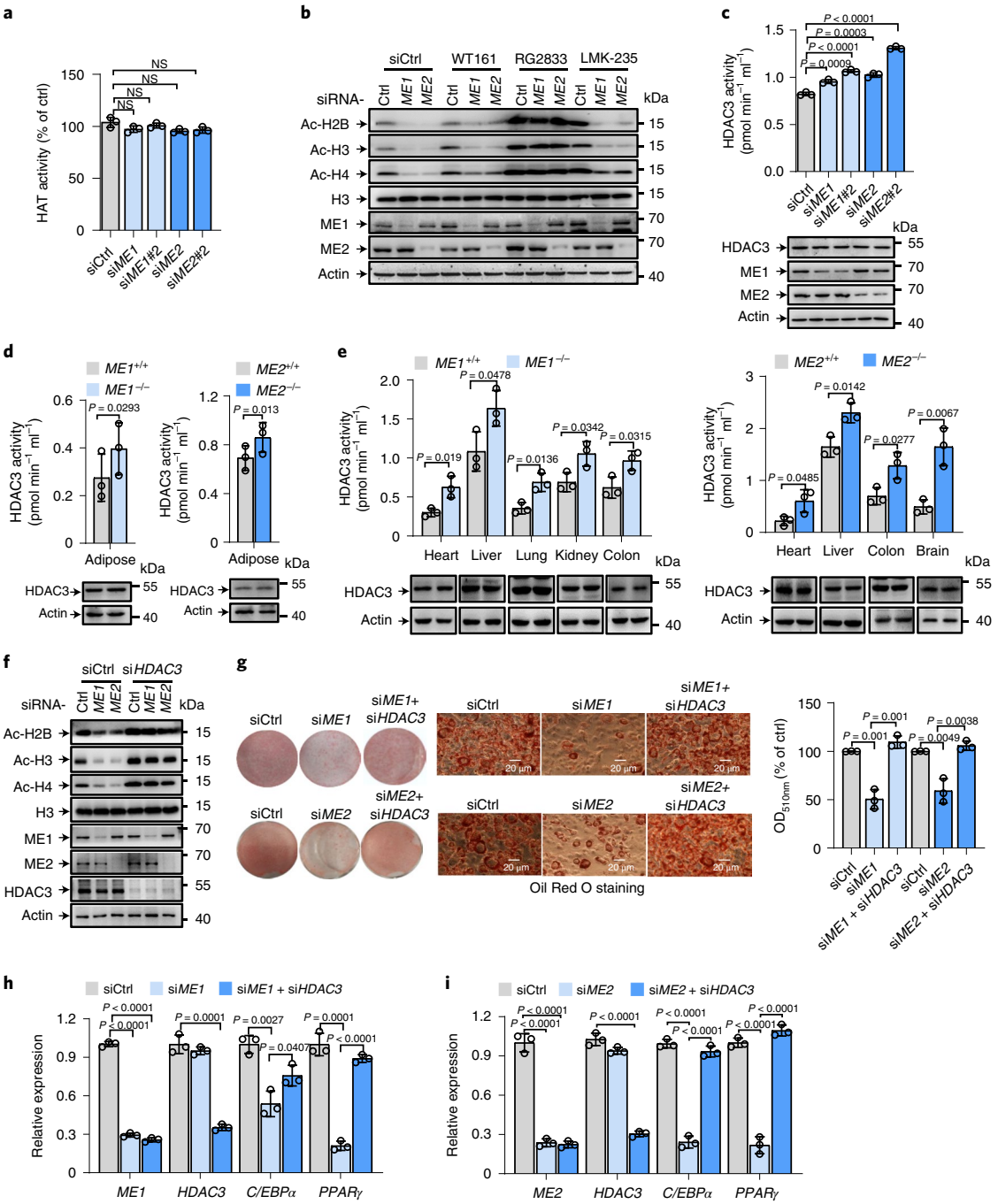

Fig. 2 | Malic enzymes regulate histone acetylation through HDAC3. a,**c**, 3T3-L1 preadipocytes transfected with control, or two sets of *ME1* or *ME2* siRNAs as indicated. Nuclear protein was extracted and HAT activity was measured (**a**). HDAC3 activity was examined (top) and protein expression was analysed (bottom; **c**). **b**, U2OS cells transfected with control, *ME1* or *ME2* siRNA as indicated were treated with different inhibitors at a concentration of 2 μM for 24 h. Protein expression was examined by western blotting. **d**,**e**, HDAC3 enzymatic activity of adipose tissue (**d**) or other tissues (**e**) from *ME1* or *ME2* knockout mice. Protein expression is shown below. **f**, 3T3-L1 preadipocytes transfected with control, *ME1*, *ME2* and/or *HDAC3* siRNAs as indicated were stimulated to differentiate for 7 d. Protein expression was detected using western blotting. **g**, 3T3-L1 preadipocytes transfected with control, *ME1*, *ME2*, and/or *HDAC3* siRNAs as indicated were stimulated to differentiate for 7 d. Cells were fixed and stained with Oil Red O (left). Images of stained cells at a higher magnification are shown (middle). Oil Red O staining was quantified (right). **h**,**i**, 3T3-L1 preadipocytes transfected with control, *ME1* (**h**), *ME2* (**i**), and/or *HDAC3* siRNAs as indicated were stimulated to differentiate for 7 d. Relative mRNA levels were analysed by quantitative PCR (qPCR). Data in **a**, **c**–**e** and **g** are from $n = 3$ biological replicates and **h** and **i** from $n = 3$ technical replicates from one of three independent experiments with similar results. Data are the mean ± s.d. Statistical significance was determined by a two-tailed unpaired *t*-test. NS, not significant. Oil Red O staining images and western blots in **b** and **c**–**g**, are representative of three independent experiments. For all western blot data, histone expression levels (Ac-H2, Ac-H3, Ac-H4 and total H3) were analysed using acid-extracted cell lysates, total H3 was used as loading control; all other protein expression levels (ME1, ME2, and HDAC3) were assessed with total cell lysates, Actin was used as loading control. The samples derived from the same experiment and the blots were processed in parallel.

notable reduction of *C/EBPα* and *PPARγ* mRNA levels, and *HDAC3* silencing was sufficient to restore *C/EBPα* and *PPARγ* expression levels to approximately WT levels (Fig. 2h,i). Likewise, inhibition of HDAC3 by RGFP966 rescued the expression of these genes in *ME1*- or *ME2*-depleted cells (Extended Data Fig. 3i). Thus, HDAC3 activation induced by *ME1* or *ME2* silencing is sufficient to impair adipocyte differentiation and adipogenic gene expression. Similarly, in proliferating tumour cells such as U2OS and human colon cancer HCT116 cells, inhibition of HDAC3 reversed the reduction of *Glut4* expression caused by *ME1* or *ME2* silencing (Extended Data Fig. 3j). Glut4 was selected for this examination because it is a well-characterized determinant that mediates adipocyte glucose consumption[14]. Collectively, suppression of HDAC3-mediated histone deacetylation is required for gene expression regulated by MEs.

Malic enzymes conduct chromatin remodelling through HDAC3. The restoration of histone acetylation by *HDAC3* silencing might render *ME*-depleted cells to reacquire the capability to conduct chromatin remodelling, thereby affecting gene expression. Chromatin immunoprecipitation (ChIP) assays using antibodies against acetylated H3 (Ac-H3) and acetylated H2B (Ac-H2B) revealed that acetylation of histones H3 and H2B at the *Adipoq*, *C/EBPα* and *PPARγ* promoters was statistically and significantly reduced in *ME1*- or *ME2*-depleted cells, and this effect was rescued by *HDAC3* depletion (Fig. 3a,b). To explore whether MEs mediated histone acetylation genome wide, we performed ChIP sequencing (ChIP–seq) analysis and found silencing of *ME* resulted in less deposition of Ac-H2B or Ac-H3 in groups of genomic loci (Fig. 3c,d), suggesting that *ME* depletion reduces histone acetylation and thus may lower gene transcription. To establish the direct connection between HDAC3 activation and the observed reduction in histone acetylation, we performed ChIP–seq experiments using an HDAC3-specific antibody. Knockdown of *ME* led to reduced HDAC3 levels localized in genomic regions (Fig. 3e). In control cells, Ac-H2B-binding regions overlapped with about 42% of HDAC3-binding regions, and the Ac-H3-binding regions overlapped with about 64% of HDAC3-binding sites (Fig. 3f), which were diminished in *ME* knockdown cells (Fig. 3g). Together, these findings reveal a role for MEs in remodelling chromatin through HDAC3-mediated histone deacetylation.

NADPH binds to HDAC3 and inhibits its activity. We further determined the mechanism by which MEs suppress HDAC3. Subcellular fraction analysis showed that ME1 and ME2 were entirely in the cytoplasmic and mitochondrial fractions, while HDAC3 was primarily in the nucleus with a modest amount of protein detected in the cytoplasmic fractions. Moreover, the subcellular localization of MEs and HDAC3 remained unchanged before (day 0) and after (day 7) differentiation induction (Extended Data Fig. 4a). These findings suggest that direct protein–protein association between MEs and HDAC3 appears unlikely to occur under these conditions. Previous studies revealed that ME is a major source of cellular NADPH[6,7], and *ME1* or *ME2* silencing decreased cellular NADPH levels significantly under both undifferentiating and differentiating conditions (day 0 and day 7; Extended Data Fig. 4b). Similar results were obtained when another set of siRNAs was used (Extended Data Fig. 4c). Notably, decreased NADPH levels were also observed in adipose tissue and other tissues from *ME* knockout mice compared to their WT counterparts (Extended Data Fig. 4d,e). We next investigated whether NADPH is a mediator of HDAC3, and if so, whether it directly modulates HDAC3 activity. An in vitro HDAC3 enzymatic activity assay with purified Flag-tagged human HDAC3 protein from mammalian HEK293T cells revealed that NADPH reduced the activity of HDAC3 in a dose-dependent manner, while Ins(1,4,5,6)P_4 as a positive control enhanced HDAC3 activity (Fig. 4a). NADPH is a phosphorylated form of NADH and exhibits a similar structure to cofactors NADH, NAD^+ and $NADP^+$. However, in sharp contrast to NADPH, none of the other cofactors affected HDAC3 enzymatic activity (Fig. 4a), suggesting that NADPH is a specific regulator of HDAC3. The inactivation of HDAC3 in vitro indicates that NADPH may be a binding partner of HDAC3. Indeed, a real-time binding assay using surface plasmon resonance (SPR) showed that NADPH was able to bind to HDAC3 with a dissociation constant (K_D) of about 1.81 μM, whereas $NADP^+$, NADH and NAD^+ showed no or less affinity towards HDAC3 (Fig. 4b). To further determine the direct binding between NADPH and HDAC3, we performed drug affinity responsive target stability (DARTS) assays and cellular thermal shift assays (CETSAs). DARTS data suggest that only NADPH, not $NADP^+$, NAD^+ or NADH, binds to and protects HDAC3 from degradation by pronase in a dose-dependent manner (Fig. 4c). In the presence of NADPH, the melting curve of HDAC3 was significantly shifted, indicating the direct binding between NADPH and HDAC3 (Fig. 4d). Taken together, these data suggest that NADPH binds to HDAC3 and inhibits its activity.

Malic enzymes affect histone acetylation through NADPH-mediated HDAC3 inhibition. We next determined whether NADPH sufficiency suppresses cellular HDAC3. To test this, we performed transfection using X-tremeGENE HP DNA Transfection reagent, which enabled us to introduce NADPH into cells efficiently. Indeed, a dose-dependent increased cellular NADPH level was observed when cells were transfected with NADPH using the X-tremeGENE system, suggesting that this method works efficiently (Extended Data Fig. 5a). Accordingly, HDAC3 activity decreased with an increasing amount of NADPH (Extended Data Fig. 5b). By contrast, HAT activity was not affected by the addition of NADPH (Extended Data Fig. 5c). To further confirm this, we examined HAT activity by incubating NADPH with nucleic extracts in vitro. Again, NADPH had no effect on HAT activity (Extended Data Fig. 5d). Unlike NADPH, transfection of NADH, NAD^+ and $NADP^+$ did not suppress HDAC3 activity (Fig. 5a,b). Consistent with these observations, addition of NADPH augmented cellular histone acetylation in a concentration-dependent manner (Fig. 5c). Moreover, *HDAC3* depletion enhanced histone acetylation and minimized the difference between cells treated with NADPH and untreated cells (Fig. 5c). These data indicate that NADPH-increased histone acetylation is dependent on HDAC3.

We next investigated if NADPH supplementation is sufficient to reverse HDAC3 activation induced by *ME* silencing. Cellular NADPH levels in *ME1*- or *ME2*-depleted cells were restored when cells were transfected with NADPH (Fig. 5d). As shown in Fig. 5e, NADPH addition decreased cellular HDAC3 activity in a dose dependent manner and reversed HDAC3 activation induced by *ME* depletion. Consistent with the effect of NADPH on HDAC3 activity, NADPH supplementation restored the levels of histone acetylation in *ME1*- or *ME2*- depleted differentiated 3T3-L1 cells (Fig. 5f). To further confirm these findings, we overexpressed G6PD, the first and rate-limited enzyme in the oxPPP, which is one of the major NADPH production routes, to increase cellular NADPH levels. Notably, enforced expression of G6PD increased the NADPH levels and restored the histone acetylation of *ME1*- or *ME2*- depleted cells (Fig. 5g). These data demonstrate that reduced HDAC3 activity and increased histone acetylation following *ME* silencing could be rescued by NADPH.

NADPH is an important factor in the cellular anti-oxidation system. To examine whether redox reactions involved in *ME1*- and *ME2*-mediated histone acetylation, we treated the cells with the ROS scavenger *N*-acetyl-L-cysteine (NAC). Cellular ROS levels were reduced with NAC treatment, while histone acetylation still decreased in *ME1* and *ME2* knockdown cells (Extended Data Fig. 5e). We next investigated whether the regulation of histone acetylation by MEs is dependent on glutathione (GSH). Although

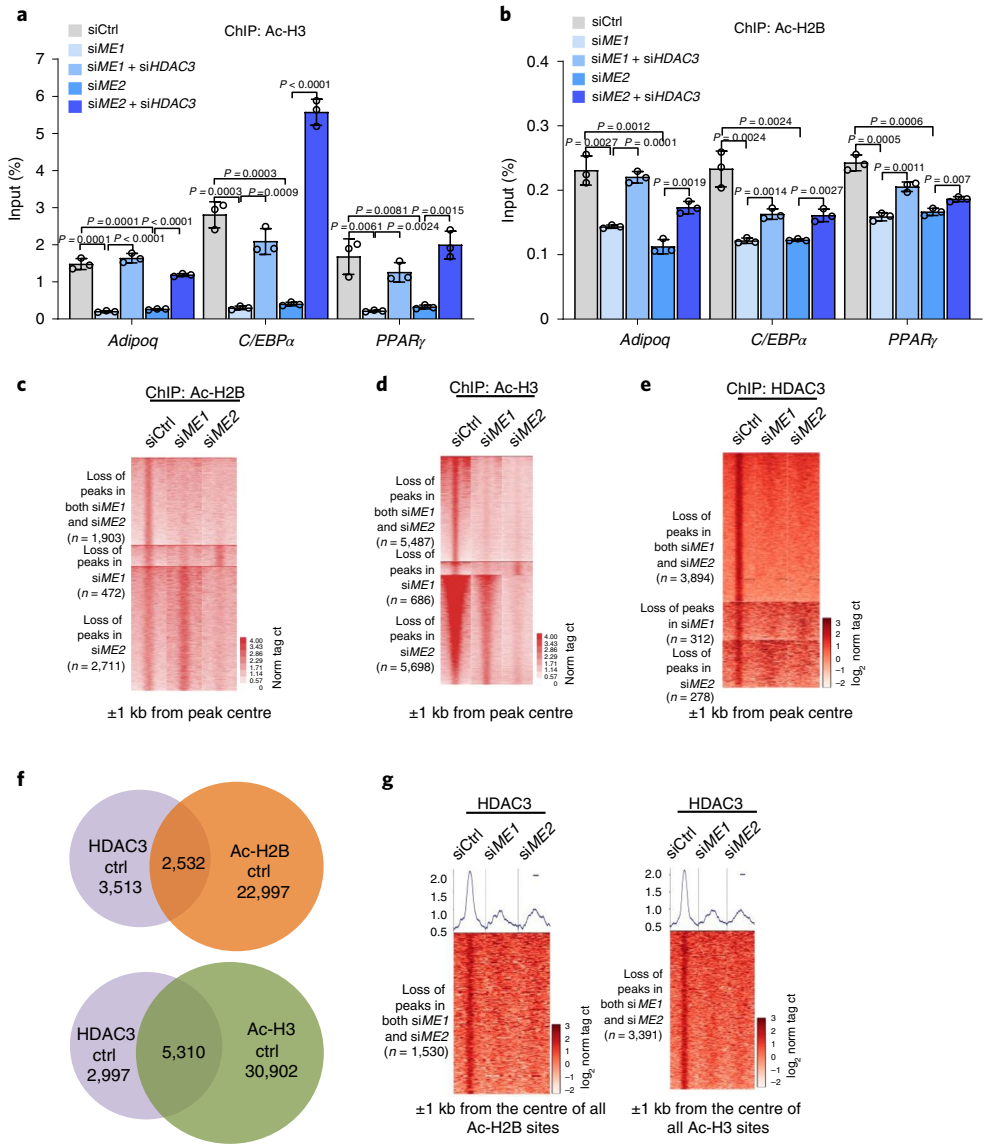

Fig. 3 | HDAC3 mediates ME-regulated gene transcription. a,**b**, The 3T3-L1 preadipocytes were transfected with control, *ME1*, *ME2* and/or *HDAC3* siRNAs as indicated and stimulated to differentiate for 7 d. ChIP analysis was performed using antibodies against Ac-H3 (**a**) and Ac-H2B (**b**). Immunoprecipitated *Adipoq*, *C/EBPα* and *PPARγ* promoter sequences were analysed by qPCR and are shown as the percentage of input. **c**–**e**, The 3T3-L1 cells were transfected with control, *ME1* or *ME2* siRNA and induced to differentiate for 7 d. Chromatin fractions were subjected to ChIP assay using Ac-H2B antibody (**c**), Ac-H3 antibody (**d**) or HDAC3 antibody (**e**). Heat map of Ac-H3/Ac-H2B/HDAC3 binding signal (rows) from −1 kb to +1 kb surrounding the centre of Ac-H3/Ac-H2B/HDAC3-binding sites for ChIP–seq tags between siCtrl, si*ME1* and si*ME2* (columns). Norm tag ct, normalized tag count. **f**, The HDAC3 cistrome largely overlapped with the Ac-H2B cistrome in control cells (top). The HDAC3 cistrome largely overlapped with the Ac-H3 cistrome in control cells (bottom). **g**, Heat map of HDAC3 at Ac-H2B (left) or Ac-H3 (right) sites from −1 kb to +1 kb surrounding the centre of HDAC3 ChIP–seq peaks in siCtrl, si*ME1* and si*ME2*. Each line represents a single HDAC3-binding site, and the colour scale indicates normalized read counts. Average signals are shown on the top. Data in **a** and **b** are from $n = 3$ technical replicates. Data are mean ± s.d. Statistical significance was determined by a two-tailed unpaired *t*-test. For ChIP–seq analysis, there were no technical replicates for anti-Ac-H2B or anti-Ac-H3 and $n = 2$ technical replicates for anti-HDAC3 ChIP–seq.

GSH supplementation restored the decreased histone acetylation in *ME1*- and *ME2*-depleted cells and upregulated cellular NADPH levels (Extended Data Fig. 5f), *ME* silencing had a minimal effect on GSH levels (Extended Data Fig. 5g), suggesting GSH may not be involved in *ME*-mediated histone acetylation. In eukaryotic cells, acetyl-CoA generated from acetate serves as the donor for acetyl groups for histone acetylation. Next, we tested if acetyl-CoA participates in histone acetylation induced by MEs during cell differentiation. As shown in Extended Data Fig. 5h, acetate supplementation failed to rescue the histone acetylation in *ME1*- and *ME2*-depleted cells, while NADPH addition increased histone acetylation even in the presence of acetate. Furthermore, to manipulate cellular NADPH levels directly, we used the TPNOX system developed by Cracan et al.[37]. TPNOX is strictly specific to NADPH by oxidizing NADPH to $NADP^+$. We overexpressed untargeted TPNOX (TPNOX) or mitochondria-targeted TPNOX (mitoTPNOX) in 3T3-L1 cells. Similarly, the reduction of cellular NADPH levels by TPNOX/mitoTPNOX overexpression led to an increase in HDAC3 enzymatic activity (Fig. 5h). Consistent with this, histone acetylation also decreased in TPNOX-expressing cells (Fig. 5i). Taken together, these data reveal that MEs modulate histone acetylation through NADPH-mediated HDAC3 inhibition.

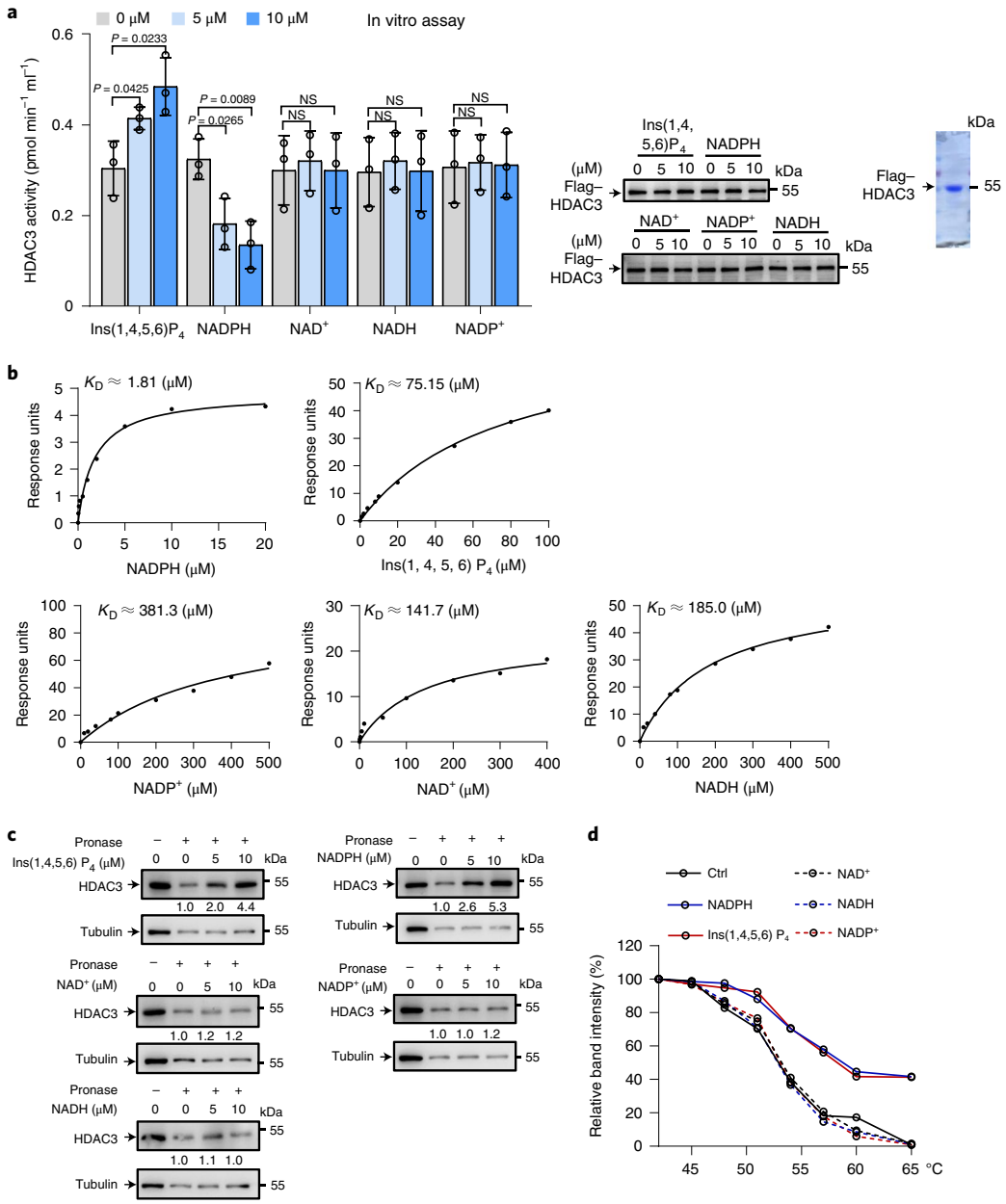

Fig. 4 | NADPH directly binds and inhibits HDAC3 in vitro. a, In vitro assay of enzymatic activity of purified Flag-tagged human HDAC3 protein from HEK293T cells after overnight incubation with increasing amounts of NADPH, $NADP^+$, NADH, NAD^+ or $Ins(1,4,5,6)P_4$. Purified Flag–HDAC3 protein was detected by western blotting and Coomassie Brilliant Blue staining. **b**, The K_D values for NADPH, $NADP^+$, NADH, NAD^+ and $Ins(1,4,5,6)P_4$ from immobilized HDAC3 were determined by SPR. A real-time graph of response units against, respectively, NADPH, $NADP^+$, NADH, NAD^+ and $Ins(1,4,5,6)P_4$ concentration is shown. **c**, Identification of the direct binding between NADPH and HDAC3 via DARTS assays (Methods). $Ins(1,4,5,6)P_4$ was a positive control. Relative HDAC3/tubulin ratios are shown. **d**, CETSAs exhibit the binding affinity of NADPH to HDAC3 in cells (Methods). $Ins(1,4,5,6)P_4$, which directly interacts with HDAC3, was a positive control. Data in **a** are from $n = 3$ biological replicates. Data are the mean ± s.d. Statistical significance was determined by a two-tailed unpaired *t*-test. In **a** (middle and right) and **c**, western blots are representative of three independent experiments.

NADPH disrupts the HDAC3–NCoR association through competition with Ins(1,4,5,6)P_4. Next, we investigated the mechanism by which NADPH represses HDAC3 activity. The enzymatic activity of HDAC3 requires recruitment into complexes with its co-activator Ncor1- or Ncor2-DAD[21]. The assembly of the complexes is largely dependent on $Ins(1,4,5,6)P_4$ and mediated by the pseudo-helix H1 and loop mutations L1 and L6 on HDAC3 (ref. [22]). Correlating with the findings that *ME1* and *ME2* depletion reduces NADPH production, silencing of *ME1* or *ME2* enhanced the HDAC3–Ncor1 or HDAC3–Ncor2 interaction at the endogenous level and NADPH addition reversed it (Extended Data Fig. 6a,b). Together, these findings prompted us to explore whether NADPH abrogates HDAC3 recruitment to DAD. To address this, we co-expressed WT HDAC3 or mutant HDAC3 constructs ($Ins(1,4,5,6)P_4$- and DAD-binding defective L1, L6 or all ('Mut-all') mutations[22]) with Ncor1-DAD in mammalian HEK293T cells in the presence or absence of NADPH. Strikingly, NADPH supplementation reduced the association between WT HDAC3 and Ncor1-DAD, but failed to affect mutant HDAC3 binding to Ncor1-DAD (Fig. 6a). Similar results were obtained with Ncor2-DAD (Fig. 6b). Addition of NADPH decreased

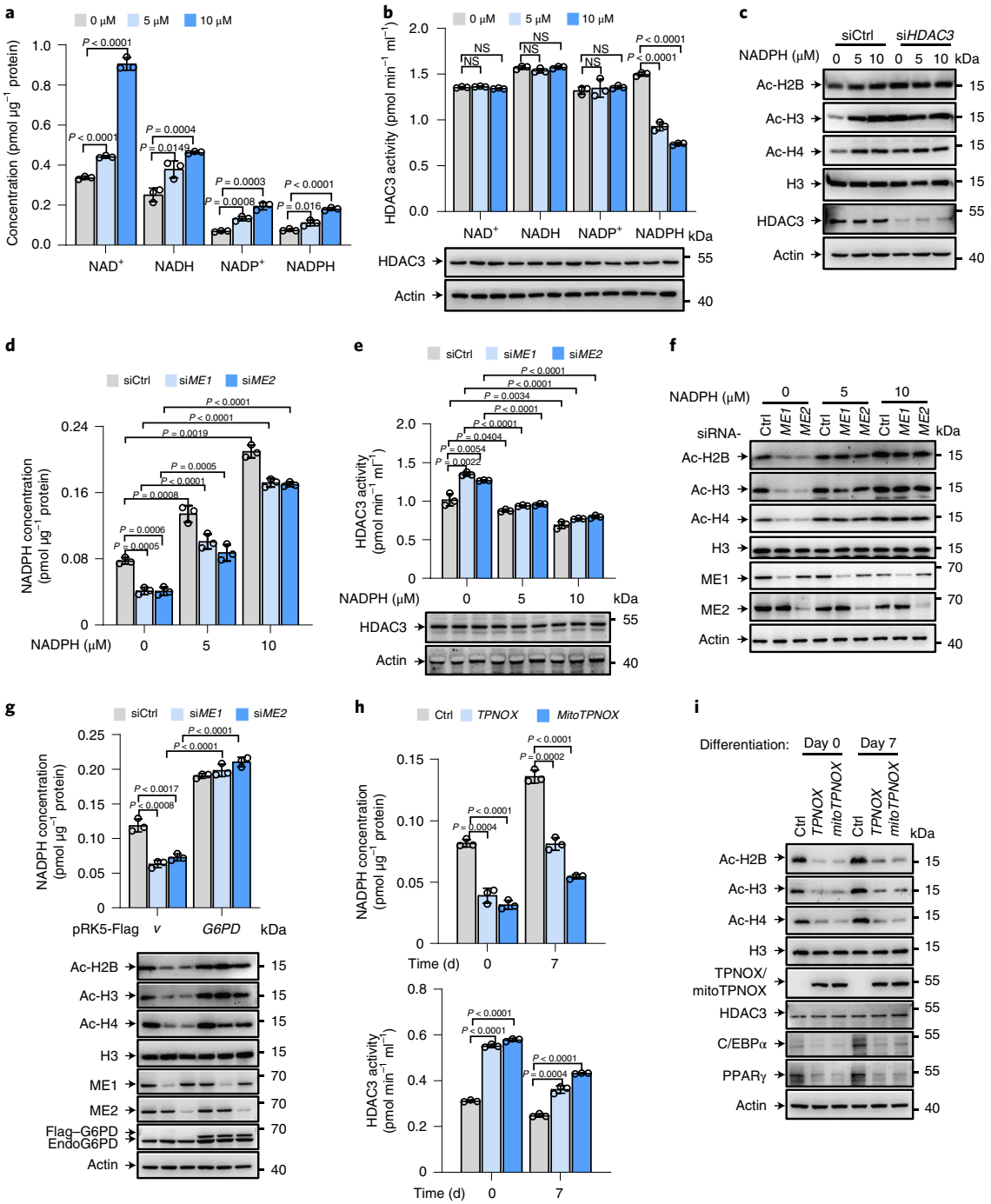

Fig. 5 | NADPH affects histone acetylation through inhibition of HDAC3. a,**b**, The 3T3-L1 preadipocytes were transfected with NAD+, NADH, NADP+ or NADPH using X-tremeGENE HP DNA Transfection reagent. Cellular NAD+, NADH, NADP+ and NADPH levels were determined (**a**). Cellular HDAC3 enzymatic activity was analysed (top). HDAC3 expression is shown below (**b**). **c**, The 3T3-L1 preadipocytes were transfected with control siRNA or *HDAC3* siRNA and treated with increasing amounts of NADPH and subjected to differentiation induction for 7 d. Protein expression was determined by western blot analysis. **d**,**e**, The 3T3-L1 preadipocytes were transfected with control, *ME1* or *ME2* siRNA and with increasing amounts of NADPH. Cellular NADPH levels were determined (**d**). Cells were lysed for assaying HDAC3 activity (top). HDAC3 expression is shown below (**e**). **f**, The 3T3-L1 preadipocytes were transfected with control, *ME1* or *ME2* siRNA and stimulated to differentiate for 7 d in the presence or absence of increasing amounts of NADPH. Protein expression was detected using western blotting. **g**, The 3T3-L1 preadipocytes were transfected with control, *ME1* or *ME2* siRNA and stimulated to differentiate for 7 d in the presence or absence of exogenous G6PD. Cellular NADPH levels were determined (top). Protein expression is shown below. **h**,**i**, TPNOX- and mitoTPNOX-expressed 3T3-L1 preadipocytes were stimulated for 7 d. NADPH levels (top) and HDAC3 activity (bottom) were examined before (day 0) and after (day 7) differentiation (**h**). Protein expression was determined by western blot analysis (**i**). Data in **a**, **b**, **d**, **e**, **g** and **h** are from $n = 3$ biological replicates. Data are the mean ± s.d. Statistical significance was determined by a two-tailed unpaired *t*-test. Western blots in **b**, **c**, **e**–**g** and **i** represent three independent experiments. For all western blot data, histone expression (Ac-H2, Ac-H3, Ac-H4 and total H3) was analysed using acid-extracted cell lysates, and total H3 was used as the loading control; all other protein expression was assessed with total cell lysates and actin used as the loading control. The samples were derived from the same experiment and blots processed in parallel.

the interaction between Ncor-DAD and WT HDAC3, but not the mutant HDAC3 (Fig. 6a,b). As the mutated amino acid residues are responsible for HDAC3 binding to Ncor-DAD and Ins(1,4,5,6)P_4 (ref. [22]), these findings suggest that NADPH may associate with HDAC3 in a way similar to that of Ins(1,4,5,6)P_4. Thus, we next investigated whether NADPH competes with Ins(1,4,5,6)P_4 to interact with HDAC3. In vitro binding assays using purified HDAC3 and Ncor1- or Ncor2-DAD revealed that NADPH reduced the HDAC3 and DAD association, and perturbed HDAC3–DAD assembly induced by Ins(1,4,5,6)P_4 (Fig. 6c,d). Similar results were found using lysates from cells expressing HDAC3 and/or Ncor1- or Ncor2-DAD. NADPH could inhibit the assembly of HDAC3 and Ncor-DAD complexes even in the presence of Ins(1,4,5,6)P_4 (Extended Data Fig. 6c,d). Likewise, NADPH transfection resulted in decreased formation of HDAC3–DAD complexes in cells, even in the presence of Ins(1,4,5,6)P_4 (Extended Data Fig. 6e,f). These findings suggest that NADPH may compete with Ins(1,4,5,6)P_4 to bind to HDAC3, as NADPH possibly has a profound effect on assembly of HDAC3–DAD complexes. To further confirm these findings, we performed real-time binding assays again using SPR. Consistently, both NADPH and Ins(1,4,5,6)P_4 were able to bind to HDAC3, with K_D values of 1.25 μM and 81.13 μM, respectively (Fig. 6e,f). Combined with previous data (Fig. 4b), these results suggest that NADPH has a high binding affinity towards HDAC3. Correlating with immunoprecipitation data, neither NADPH nor Ins(1,4,5,6)P_4 showed a binding affinity towards mutant HDAC3 (Extended Data Fig. 6g–i).

To gain further insight into the structural basis for the inhibition of HDAC3 by NADPH, we conducted docking experiments of HDAC3 by AutoDock Vina[38] using Ins(1,4,5,6)P_4 or NADPH as the ligand. To evaluate the accuracy of docking, we first docked Ins(1,4,5,6)P_4 into the crystal structure of HDAC3–DAD–Ins(1,4,5,6)P_4 complex with Ins(1,4,5,6)P4 molecule removed beforehand. When the searching box covered the whole surface of HDAC3 and DAD, Ins(1,4,5,6)P4 was found to dock into multiple regions on the surface of HDAC3. To increase the accuracy of docking, we reduced the searching box to focus on the space around residues H17, G21, K25, R265 and R301 (ref. [22]), as mutations made to these sites significantly suppressed the binding of Ins(1,4,5,6)P_4 or NADPH to HDAC3. Indeed, the binding pose of Ins(1,4,5,6)P_4 with the highest score was very similar to that in the HDAC3–DAD–Ins(1,4,5,6)P_4 crystal structure (Extended Data Fig. 7a; root mean squared deviation = 0.88 Å) and shows binding energy of −6.8 kcal mol^{-1} (Supplementary Table 1). Further examination revealed that, in the docked structure and the crystal structure, Ins(1,4,5,6)P_4 shared the same set of polar interactions with the protein complex (Extended Data Fig. 7b). This result can be robustly reproduced when repeating the docking procedure.

Next, Ins(1,4,5,6)P_4 and NADPH were docked into HDAC3 only. In both cases, the blind docking with the large search box led to binding poses in multiple regions (Extended Data Fig. 7c,d). Among these regions, the binding interface between HDAC3 and Ins(1,4,5,6)P_4 in the crystal structure (referred to as BI zone hereinafter) is likely the binding site for both Ins(1,4,5,6)P_4 and NADPH, because this zone is the only region rich in positive charges on the HDAC3 surface, and both Ins(1,4,5,6)P_4 and NADPH have multiple phosphate groups. This assumption is supported by the in vivo experimental evidence, and is further confirmed by the in vitro binding assays after mutation, as discussed above. Therefore, we limited the docking to this region as well, and ran AutoDock Vina in triplicate, yielding 27 poses for each ligand. The result showed that, in the absence of DAD, the binding of Ins(1,4,5,6)P_4 to the BI zone of HDAC3 was weaker than that of NADPH, as indicated by less negative binding energy (−5.1 kcal/ mol^{-1}) for the former and more favoured energy for the latter (−7.2 kcal mol^{-1}; Supplementary Tables 2 and 3). The result of the binding energy should not be emphasized though, because the current docking algorithms cannot predict the binding energy reliably, underscoring the importance of performing docking under the guidance of the experimental evidence. We inspected all poses that fall into the BI zone, specifically 1 pose for Ins(1,4,5,6)P_4 and 11 poses for NADPH. When artificially adding the crystal structure of DAD into the docked HDAC3, the pose of Ins(1,4,5,6)P_4 did not overlap with DAD. In contrast, all poses of NADPH showed crashing with DAD, as illustrated by the most energetically favoured pose in the BI zone (Fig. 6g,h and Extended Data Fig. 7e). To understand why NADPH is more favoured than Ins(1,4,5,6)P_4 for binding with HDAC3, interactions in the protein–ligand interface were visualized using Maestro (Extended Data Fig. 7f). As expected, NADPH formed five salt bridges or hydrogen bonds with HDAC3, while Ins(1,4,5,6)P_4 formed only two. We also conducted docking for NAD^+, NADH and $NADP^+$ (Extended Data Fig. 7g). NADH and $NADP^+$ showed weaker binding compared to NADPH, largely in line with the experimental binding assay. However, NAD^+ exhibited tighter binding than NADPH, and the binding energies of the three ligands were all lower than those of Ins(1,4,5,6)P_4. These discrepancies between the docking result and the in vitro binding assay could be attributed to the limited accuracy of the docking method.

Since the docking method is not quantitively reliable, we resorted to molecular dynamics (MD) simulations to check whether the predicted binding poses of NADPH can stably reside in the binding pocket. To this end, a 500-ns MD trajectory was recorded using the most favourable pose of NADPH in complex with HDAC3 (Fig. 6g,h) as the initial conformation. Indeed, the NADPH kept staying in the BI zone and made contacts readily with K25, R265 and R301 during the simulation (Supplementary Video). A previous MD study suggests the dynamics of Tyr 298 in HDAC3 might play an important role in substrate recognition[39]. In the apo form of HDAC3, Tyr 298 is in an equilibrium of two rotameric states. The

Fig. 6 | NADPH binds to HDAC3 and abrogates assembly of HDAC3–DAD complexes. a,**b**, HEK293T cells transfected with HA-tagged DAD (Ncor1) (**a**) or HA-tagged DAD (Ncor2) (**b**) and Flag-tagged HDAC3 or mutant HDAC3 were treated with or without 20 μM NADPH for 48 h. Cell lysates were immunoprecipitated with an anti-Flag (M2) antibody. Immunoprecipitated protein (IP) and 5% input were analysed by western blot. L1 is 17C/G21A/K25I, L6 is R265P/L266M and 'Mut-all' is H17C/G21A/K25I/R265P/L266M/R301A. **c**,**d**, In vitro binding assays of bacterially expressed GST-HDAC3 and purified Flag–DAD (Ncor1) (**c**) or Flag–DAD (Ncor2) (**d**) from HEK293T cells in the presence or absence of NADPH and/or Ins(1,4,5,6)P_4. **e**,**f**, The K_D value for immobilized HDAC3 from NADPH (**e**) or Ins(1,4,5,6)P_4 (**f**), were determined by SPR. Independent replicates of the same binding assay shown in Fig. 4b (top). **g**,**h**, Electrostatic surface representation of the HDAC3 onto which NADPH docks. The most energetically favoured pose of NADPH in the potential binding pocket was predicted by AutoDock Vina (v1.1.2) and shown in stick view (**g**) The zoom-in structure showing interaction details between HDAC3 and NADPH. The labelled residues are mutation sites of the three mutants designed to inhibit binding of Ins(1,4,5,6)P_4 and NADPH (**h**). **i**, Control or *HDAC3* siRNA-transfected U2OS cells were transfected with RNAi-resistant WT or mutant (L6) HDAC3 for 24 h and then were treated with increasing amounts of NADPH for another 24 h. Protein expression is shown. **j**, U2OS cells were transfected with control, *ME1* and *ME2* and/or *HDAC3* siRNA for 24 h, after which cells were transfected with WT or mutant (L6) HDAC3 for another 24 h. Protein expression is shown. Western blots in **a**–**d**, **i** and **j** represent three independent experiments. For western blot data, histone expression was analysed using acid-extracted cell lysates, and total H3 was used as the loading control; all other protein expression was assessed with total cell lysates and actin used as the loading control. The samples were derived from the same experiment and gels/blots processed in parallel.

binding of Ins(1,4,5,6)P_4 and DAD made the side chain of Tyr 298 favour an 'inward' state, which could be necessary for recognizing the substrate. We performed MD simulations of HDAC3 in the apo form and two bound forms (HDAC3–Ins(1,4,5,6)P_4 and HDAC3–DAD–Ins(1,4,5,6)P_4) and achieved similar results. Interestingly, we found that binding of NADPH significantly shifted the population of the Tyr 298 side chain towards an alternative rotameric state (Extended Data Fig. 8), prompting a possible mechanism for inhibition of HDAC3 activity by NADPH.

These results are in good agreement with experimental binding assays discussed above and further suggest NADPH could compete with Ins(1,4,5,6)P_4 and lead to the dissociation of DAD from HDAC3. Thus, these findings suggest that NADPH functions in suppressing HDAC3 recruitment of Ncor-DAD by interrupting the interaction between HDAC3 and Ncor-DAD or Ins(1,4,5,6)P_4.

To better evaluate whether the binding between NADPH and HDAC3 is required for NADPH-mediated inhibition of HDAC3, we transfected *HDAC3*-depleted cells with WT HDAC3 or mutant HDAC3 (L6) that lost the binding affinity to NADPH. Notably, NADPH addition enhanced histone acetylation in cells expressing WT HDAC3 but not mutant HDAC3 (Fig. 6i). Similarly, the silencing of *ME1* and *ME2* failed to decrease histone acetylation in

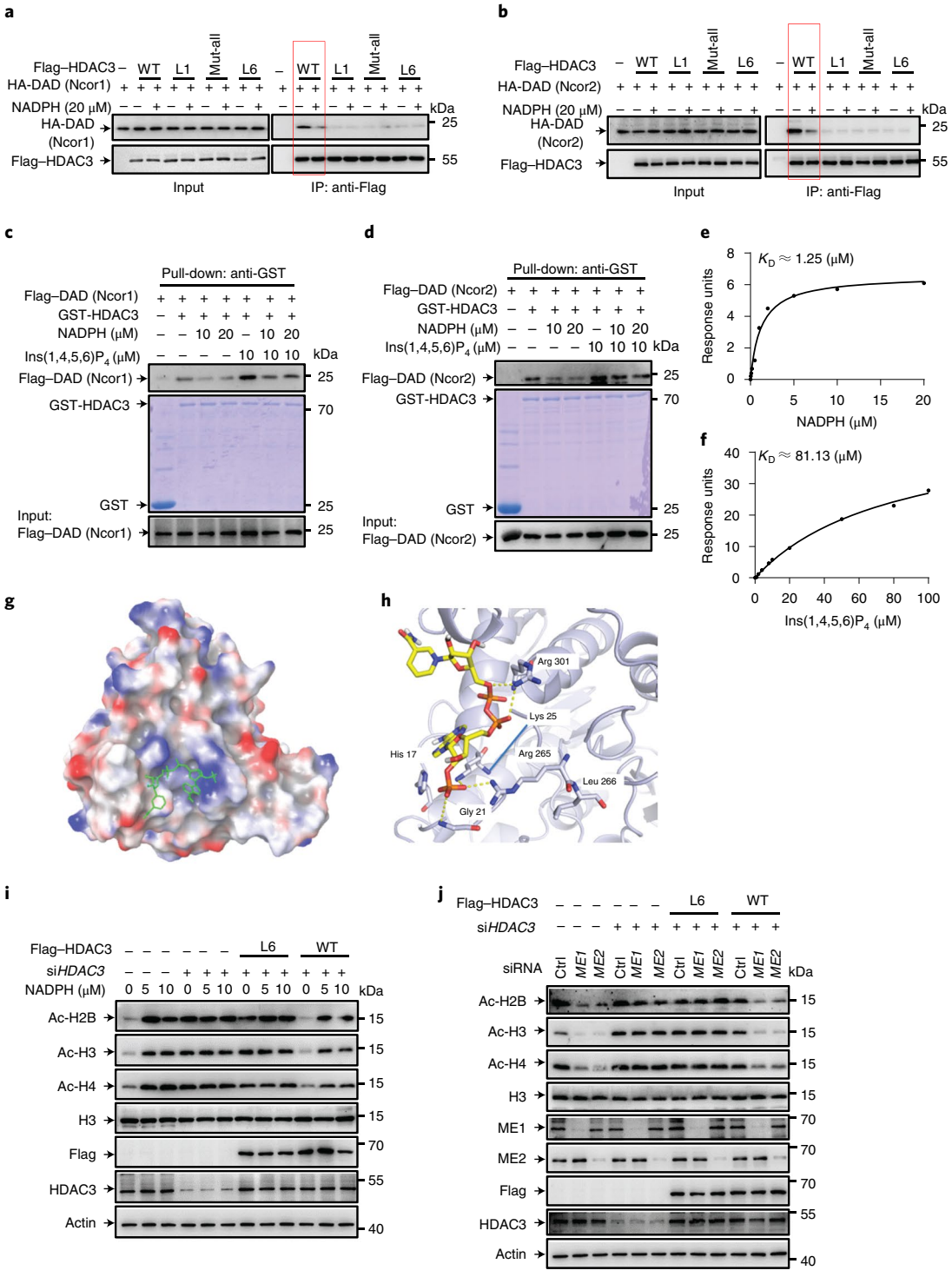

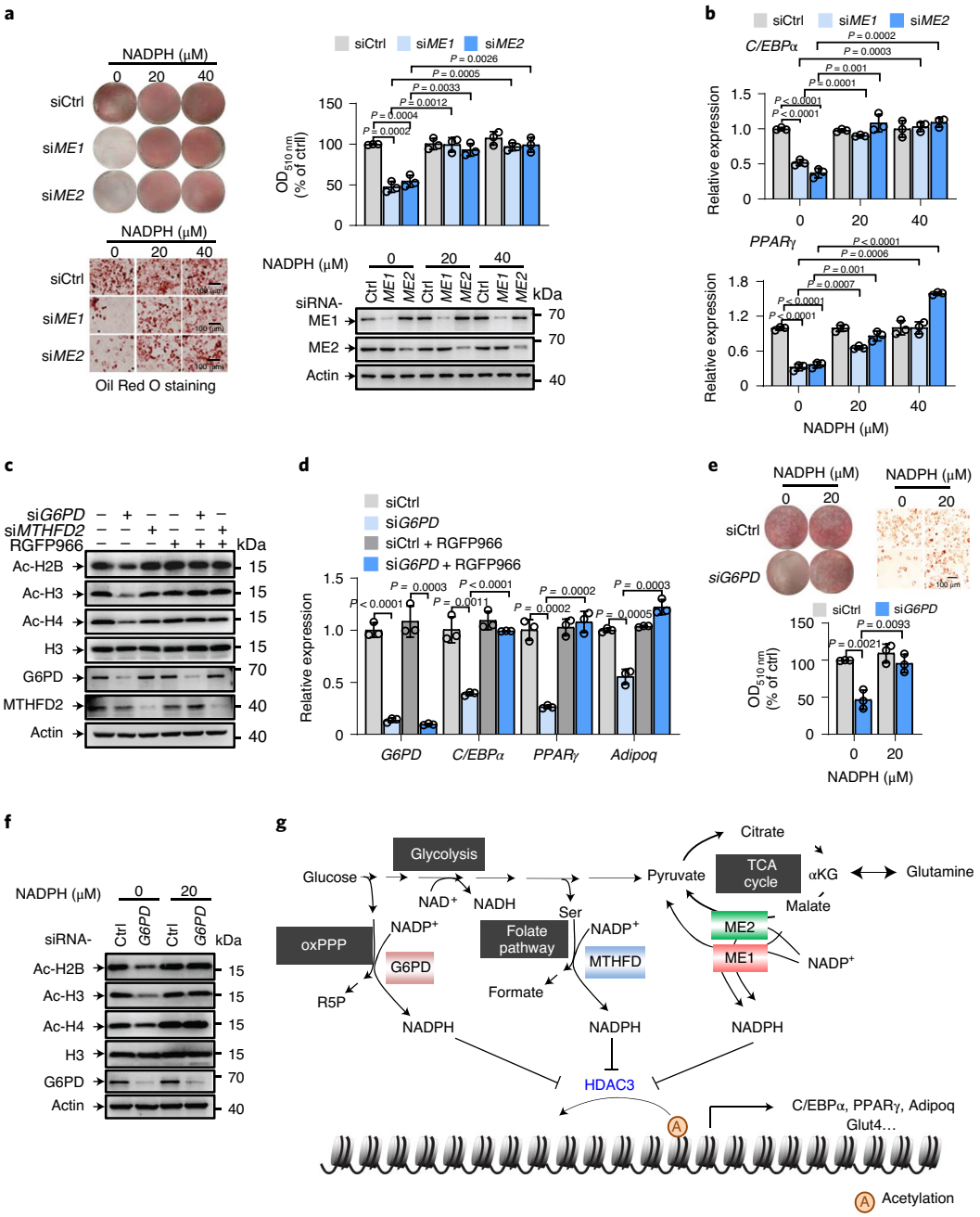

Fig. 7 | NADPH change reprograms histone acetylation and transcription. a,**b**, The 3T3-L1 preadipocytes were transfected with control, *ME1* or *ME2* siRNA and stimulated to differentiate for 7 d in the presence or absence of increasing amounts of NADPH. The accumulation of lipid droplets was assessed by Oil Red O staining (left) and quantified (right). Protein expression is shown below (**a**). RNA was extracted and relative expressions of *C/EBPα* and *PPARγ* were analysed by qPCR (**b**). **c**, The 3T3-L1 preadipocytes were transfected with control, *G6PD* or *MTHFD2* siRNA and induced to differentiate for 7 d in the presence or absence of 10 μM RGFP966. Protein expression levels were analysed by western blotting. **d**, mRNA expression of 3T3-L1 preadipocytes transfected with control or *G6PD* siRNA in the presence or absence of 10 μM RGFP966 after differentiation for 7 d. **e**,**f**, The 3T3-L1 preadipocytes were transfected with control or *G6PD* siRNA and stimulated to differentiate for 7 d in the presence or absence of 20 μM NADPH. **e**, The accumulation of differentiation-induced lipid droplets was visualized by Oil Red O staining (top) and quantified (bottom). **f**, Protein expression was analysed by western blotting. **g**, HDAC3 sensed NADPH homeostasis and linked NADPH metabolism to epigenetic changes and transcriptional regulation. αKG, α-ketoglutarate; R5P, ribose-5-phosphate; TCA, tricarboxylic acid. Data in **a** and **e** are from $n = 3$ biological replicates and **b** and **d** from $n = 3$ technical replicates from one of three independent experiments with similar results. Data are mean ± s.d. Statistical significance was determined by two-tailed unpaired *t*-test. In **a**, **c**, **e** and **f**, Oil Red O staining images and western blots represent three independent experiments. For all western blot data, histone expression was analysed using acid-extracted cell lysates, and total H3 was used as the loading control; all other protein expression was assessed with total cell lysates, and actin was used as the loading control. The samples were derived from the same experiment and blots processed in parallel.

the presence of mutant HDAC3 (Fig. 6j). Together, these data indicate that direct interaction with HDAC3 is required for NADPH to modulate histone acetylation.

Disruption of NADPH homeostasis alters histone acetylation and gene expression. Next, we investigated whether NADPH-dependent inhibition of HDAC3 underlies the mechanism

responsible for the regulation of adipocyte differentiation and adipogenic genes expression by MEs. Using Oil Red O staining to assess differentiation-induced lipid droplet accumulation, we found that cells devoid of *ME1* or *ME2* contained visibly less lipid than control cells, and NADPH supplementation restored the lipid accumulation in these cells (Fig. 7a). Similar results were obtained with different sets of *ME* siRNAs (Extended Data Fig. 9a,b). Consistent with the effect of NADPH on differentiation, exogenous NADPH rescued the expressions of *C/EBPα* and *PPARγ* in *ME1- or ME2*-depleted cells in a dose-dependent manner (Fig. 7b). Collectively, NADPH-mediated HDAC3 inhibition is required for ME-induced histone acetylation and adipocyte differentiation.

Besides MEs, the other major routes to produce NADPH are G6PD, and MTHFD in some types of cells examined[4,6]. We next assessed the generalizability of our findings by assaying the effect of NADPH alteration induced by suppression of these NADPH-producing enzymes on histone acetylation. Similar to *ME* knockdown, *G6PD* silencing in differentiated 3T3-L1 cells reduced histone acetylation and adipogenic gene expression (Fig. 7c,d). Furthermore, G6PD inhibition by 6-aminonicotinamide significantly impaired histone acetylation and resulted in suppressed adipocyte differentiation (Extended Data Fig. 9c). These effects correlated with the decrease in NADPH levels and increase in the $NADP^+$/NADPH ratio in *G6PD*-depleted 3T3-L1 cells (Extended Data Fig. 9d,e). However, both NADPH production and the $NADP^+$/NADPH ratio were nearly unaffected by folate metabolism in 3T3-L1 cells during differentiation (Extended Data Fig. 9d,e)[7]. Consistent with this, the silencing of *MTHFD2* had a minimal effect on histone acetylation in these cells (Fig. 7c). Notably, inhibition of HDAC3 by RGFP966 rescued the levels of both histone acetylation and adipogenic gene expression mediated in *G6PD*-depleted cells (Fig. 7c,d). Moreover, NADPH addition increased differentiation-induced lipid accumulation and restored the levels of histone acetylation in *G6PD*-depleted cells (Fig. 7e,f). In some tumour cells, folate metabolism, like MEs and G6PD, contributes to NADPH production[4,6]. As expected, the silencing of *MTHFD2* led to an increased $NADP^+$/NADPH ratio in U2OS and HCT116 cells (Extended Data Fig. 9f,g). Consistent with the effect of MTHFD2 on $NADP^+$/NADPH ratio, *MTHFD2* depletion reduced the levels of histone acetylation as well as *G6PD* knocking down (Extended Data Fig. 9h). Thus, modulation of HDAC3-mediated histone deacetylation may be a widespread mechanism for the regulation of gene expression by NADPH (Fig. 7g).

Discussion

NADPH is well known as an electron carrier for redox control and a substrate for biosynthetic reactions. Here we show that NADPH has a previously unidentified role in modulating epigenetic changes, which may lead us to reconsider how NADPH exactly functions in mammalian cells. For example, NADPH production by MEs in adipocytes was presumed to support differentiation by acting as a substrate for lipid biosynthesis[6,7]. In this work, however, our findings suggest an alternative mechanism for the stimulation of adipocyte differentiation by NADPH sufficiency at the transcriptional level. Additionally, by selective inhibition of each of the NADPH-producing pathways, we observed a significant correlation between the changes in histone acetylation and NADPH levels. Of note, unlike some cancer cells in which folate metabolism is one of the major routes for NADPH production[4,6], preadipocytes predominantly rely on MEs and the oxPPP for NADPH synthesis. As a result, folate metabolism has little effect on NADPH in these cells[7]. In agreement with these observations, knockdown of *MTHFD2* showed no impact on histone acetylation (Fig. 7c). Thus, these findings may reveal a common model for transcription regulation mediated by NADPH change. Given that various stresses, including metabolic stresses or genotoxic stresses such as DNA damage, affect NADPH production or usage, NADPH changes induced by these stresses may not only alter cellular biosynthetic reactions and redox status but also induce cellular responses via HDAC3-mediated gene transcription. Thus, broad considerations should be made when targeting NADPH metabolic pathways in the treatment of cancers or other diseases.

The mechanism for NADPH regulation of epigenetics and gene expression seems to be mediated by its competition with Ins(1,4,5,6)P_4 for binding HDAC3. In vitro binding assays and docking studies reveal that NADPH exhibits a higher affinity towards HDAC3 compared to Ins(1,4,5,6)P_4. Thus, it is tempting to speculate that proliferating cells sensitize to NADPH dynamic for gene expression. These observations may greatly contribute to the understanding of why NADPH is a 'limiting step' for cell proliferation[2]. Nevertheless, a previous study reported that NADPH serves as an activator of recombinant HDAC1 and HDAC2 in vitro[40], suggesting that NADPH may have selective effects on HDAC family members. Meanwhile, exactly how NADPH acts on HDAC3 needs further clarification.

HDAC3 has been implicated in many important physiological events such as the regulation of circadian metabolic gene expression and the control of circadian rhythm[41,42]. Therefore, via HDAC3, disruption of NADPH homeostasis may aberrantly impact circadian clock gene expression and result in abnormal circadian behaviour, at least partially explaining the previous observation that oxPPP dysregulation changes clock gene expression[43]. In sum, NADPH may have more broad impacts on cell physiology through the control of epigenetic status and transcription.

Methods

Antibodies and reagents. Antibodies against ME1 (ab97445; dilution: 1/1,000), ME2 (ab139686; dilution: 1/1,000), Ncor2 (ab5802; dilution: 1/500) and HDAC3 (ab7030; dilution: 1/3,000) were purchased from Abcam (Cambridge). Ncor1 (NB100-58842; dilution: 1/500) was purchased from Novus. Ac-H3 (06-599; dilution: 1/3,000) and Ac-H2B (07-373; dilution: 1/3,000) were purchased from Millipore (Temecula). Ac-H4 (06866; dilution: 1/3,000) was purchased from Active Motif. The HDAC1 (34589S; dilution: 1/1,000), HDAC2 (2540S; dilution: 1/1,000), HDAC4 (2072S; dilution: 1/1,000), HDAC6 (7612S; dilution: 1/1,000), C/EBPα (8178; dilution: 1/500), PPARγ (2443; dilution: 1/500), FABP4 (2120; dilution: 1/1,000) and total histone H3 (9715; dilution: 1/3,000) antibodies were ordered from Cell Signaling Technology. The HDAC5 (sc-133106; dilution: 1/200) antibodies were ordered from Santa Cruz Biotechnology. The anti-Flag (A8592) and anti-HA (3F10) agaroses were purchased from Sigma-Aldrich. Anti-β-actin (66009-1; dilution: 1/3,000) and anti-β-tubulin (10094-1-AP; dilution: 1/3,000) were from Proteintech. The following reagents were purchased from Sigma: NADPH (5130), $NADP^+$ (N5755), NAD^+(N8285), NADH (N4505), insulin (I0305000), rosiglitazone (D1515), dexamethasone (D4902), isobutylmethylxanthine (I5879), 6-aminonicotinamide (A68203) and Oil Red O (00625). TSA (S1045), nicotinamide (VB3, S1899), RGFP966 (S7229), WT161 (S8495), RG2833 (S7292) and LMK-235 (S7569) were purchased from Selleck. 2,6-di-*O*-butyryl-Ins(1,4,5,6)P_4/PM (Q-M1456) was purchased from Echelon and X-tremeGENE HP DNA Transfection Reagent (A06366236001) was purchased from Roche Diagnostics.

Animals. $ME1^{fl/fl}$ mice were produced from C57BL/6J embryonic stem cells with loxP sites flanking exon 4 to exon 5. $ME2^{fl/fl}$ mice were produced from C57BL/6J embryonic stem cells with loxP sites flanking exon 3. The $ME^{fl/fl}$ mice were then crossed with EIIa-Cre mice to generate ubiquitous *ME* knockout mice. WT and knockout C57BL/6J mice aged 12–16 weeks were euthanized and examined. Only males were used for all experiments. Mice were litter mates and assigned randomly to experimental groups. All procedures followed the guidelines of the Institutional Animal Care and Use Committee of the Institute of Basic Medical Sciences Chinese Academy Medical College.

Cell culture and transfection. HCT116 colon cancer cells and HEK293T human embryonic kidney cell lines were cultured in DMEM (Life Technologies, Invitrogen) medium containing 10% FBS (Gemini). U2OS cells were grown in McCoy's 5A medium (Gibco) supplemented with 10% FBS. The 3T3-L1 preadipocytes were kindly gifted by C. B. Thompson and maintained in DMEM with 10% CS. All cells were maintained in standard culture conditions without any antibiotic. All cell lines were subjected to the examination of mycoplasma contamination and were cultured for no more than 2 months, and their morphology was confirmed periodically to avoid cross-contamination or misuse of cell lines. No cell lines used in this work were listed in the ICLAC database. All of the siRNAs were transfected using Lipofectamine RNAiMAX Transfection Agent (Life Technologies, Invitrogen) and the small molecules (NADPH or Ins(1,4,5,6)P_4) using X-tremeGENE HP DNA Transfection Reagent.

siRNA sequences were: control siRNA: CGUACGCGGAAUACUUCGA; m*ME1*#1 siRNA: GGUGUUUGCCCAUGAACAU; m*ME1*#2 siRNA: GGCAACAAUUCCUACGUGU; m*ME1*#3 siRNA: GGCCACUGUUUAUCCUGAA; m*ME2*#1 siRNA: GCCUUACGAUUCCAUAGAA; m*ME2*#2 siRNA: GCGGCCCAAAGAGUUAUUA; m*ME2*#3 siRNA: CCAAGGAAACAAUGCAUAU; h*ME1* siRNA: GGAAGCCAAGAGGUCUCUUTT; h*ME2* siRNA: GCCAGUGAAACUUACAGAUTT; m*p53* siRNA: GTACTCTCCTCCCCTCAAT; m*G6PD* siRNA: CCACCAAGCUGAUACACACAUAUUU; mMTHFD2 siRNA: GCCGUUGUCAUUUCUGGAA; h*G6PD* siRNA: CAGUCGGAUACACACAUAUTT; hMTHFD2 siRNA: GCAACAGAGAUGAUUCCAATT; m*HDAC3* siRNA: GUCCUGCAUUAUGGUCUCUTT; h*HDAC1* siRNA: CCGGUCAUGUCCAAAGUAATT; h*HDAC2* siRNA: GAUCGUGUAAUGACGGUAUTT; h*HDAC3* siRNA: CCAAGAGUCUUAAUGCCUUTT; h*HDAC4* siRNA: GCAGCAGCAUCAGCAGUUUTT; h*HDAC5* siRNA: GGAGAGCUCAAGAAUGGAUTT; and h*HDAC6* siRNA: GCAAUGGAAGAAGACCUAATT.

NADPH transfection. For NADPH transfection in 3T3-L1 preadipocytes, cells were seeded into a six-well or 60-mm dish and cultured in DMEM containing 10% CS for 24 h. Then, 40%–50% confluent cells were changed with fresh DMEM containing 10% CS. Before transfection, 5 μM NADPH was diluted with 200 μl Opti-MEM (31985070, Life Technologies, Invitrogen) in the sterile tube and mixed gently. Afterwards, 5 μl X-tremeGENE HP DNA Transfection Reagent (Roche, A06366236001) was pipetted into the tube without directly contacting with plastic walls. The transfection complex was subsequently gently mixed and incubated for 15–30 min at room temperature (RT) and then added into cells in a drop-wise manner. Cellular NADPH levels were measured after 24–48 h of incubation.

CRISPR–Cas9-mediated deletion of *ME1* or *ME2*. Complementary oligonucleotides were annealed and inserted into the lentiCRISPR v2 vector, which encodes both Cas9 and single guide RNA (sgRNA) of interest. sgRNAs targeting *ME1* or *ME2* were designed. The sgRNA sequences used were: sgm*ME1* forward: 5′-CACCGCTTTATTAGTATCCATGACA -3′; reverse: 5′-AAACTGTCATGGATACTAATAAAGC-3′; sgm*ME2* forward: 5′-CACCGACTGTTCTATAGAATCCTGC-3′; reverse: 5′-AAACGCAGGATTCTATAGAACAGTC-3′.

Differentiation of 3T3-L1 preadipocytes. Approximately 4×10^4 or 1×10^5 3T3-L1 preadipocytes were seeded into a 12- or 6-well assay plate, respectively, and cultured in DMEM containing 10% CS. Each treatment was prepared in triplicate. The next day, cells were transfected with control, *ME1*, *ME2* and/or *HDAC3* siRNAs using lipofectamine RNAiMAX. NADPH transfection was performed using X-tremeGENE HP DNA Transfection reagents according to the manufacturer's instructions, 24 h after siRNA transfection. Two days after siRNA transfection, confluent cells were stimulated with differentiation cocktail containing 500 μM isobutylmethylxanthine, 1 μM dexamethasone, 1 μM rosiglitazone and 1 μg ml^{-1} insulin in DMEM with 10% FBS, to induce differentiation to adipocytes. Cells were treated with the cocktail for 4 d and then cultured in medium containing 1 μg ml^{-1} insulin for another day. Then cells were cultured in normal DMEM with 10% FBS for one more day and collected for experimental analysis.

Oil Red O staining. To make stocking buffer, 0.5 g Oil Red O was dissolved in 100 ml isopropanol and filtered using a 0.22-μm filter. Working solution was generated by mixing six parts stock with four parts H_2O, incubating for 30 min at RT and then filtering through a 0.22-μm PES filter. Cells were washed with PBS and fixed with 4% paraformaldehyde for 1 h at RT. Then cells were washed three times in PBS and stained with working solution for 10 min at 37 °C. After staining, cells were washed three times in PBS and subjected to image capture. The staining was quantified by adding isopropanol to dissolve Oil Red O and measuring the optical density at 510 nm.

Chromatin immunoprecipitation assay. Briefly, 3T3-L1 preadipocytes were transfected with control, *ME1*, *ME2* and/or *HDAC3* siRNAs as indicated and 2 d later induced to adipocytes. After another 7 d, cells were washed in PBS and subsequently cross-linked with 1% formaldehyde solution at RT for 15 min. After washed in cold PBS, the cross-linking reaction was stopped by the addition of 0.125 M glycine with gentle shaking for 5 min. Cells were then centrifuged and lysed in 300 μl SDS lysis buffer (50 mM Tris-HCl (pH 8.0), 10 mM EDTA (pH 8.0), 1% SDS and protease inhibitors) for 15 min on ice. Cell lysates were sonicated to generate DNA fragments approximately 200–1,000 bp in size and cells were subjected to immunoprecipitation with indicated antibodies against Ac-H2B, Ac-H3 or HDAC3. Immunoprecipitations were carried out overnight, and samples were then washed with low-salt buffer, high-salt buffer, LiCl salt buffer and TE buffer sequentially. Histone–DNA complexes were eluted using elution buffer (1% SDS and 100 mM $NaHCO_3$), incubated at 65 °C overnight in the presence of 0.54 M NaCl. The next day, DNase-free RNase (10 mg ml^{-1}) was added into samples and incubated for 1 h at 37 °C. Samples were then incubated with Proteinase K for another 1 h at 55 °C. Finally, DNA was purified using Qiaex II beads (Qiagen), analysed by qPCR and plotted using GraphPad Prism (v8.0). The primer sequences were: m*Adipoq*-F: ATGCCTGAACCACACAGCTTCA; m*Adipoq*-R: AGGGGTCAGGAGACCTCCCTTT; m*C/EBPα*-F: CTGGAAGTG GGTGACTTAGAGG; m*C/EBPα*-R: GAGTGGGGAGCATAGTGCTAG; m*PPARγ*-F: GTGCTTTATGGCTTGGGATT; and m*PPARγ*-R: TCTTGACCTCC TCGCGTCCCTTA.

For ChIP–seq analysis, briefly, 3T3-L1 cells were treated with siRNA for 2 d and confluent cells were induced to differentiate into adipocytes. Cells were cross-linked, and the cell lysates were sonicated to generate DNA fragments and subjected to immunoprecipitation using Ac-H2B, Ac-H3 or HDAC3 antibodies as described above. Bound DNA fragments were eluted for ChIP–seq library construction and sequencing.

ChIP–seq data processing. Raw ChIP–seq data were aligned to the mm8 build of the mouse genome using BWA software (v0.7.15)[44]. Only the sequences with mapping quality higher than 25 were kept for further analysis. Then, all mapped reads were sorted by SAMtools (v1.9)[45] with the options '--f 2 --q 10 --b --@ 20'. Peak calling for ChIP–seq data was carried out by MACS2 (v2.1.1)[46] with the parameters '--g mm --p 0.005 --nomodel --extsize 189 --call-- summits'. The overlapping and unique peaks for two sets of DNA binding sites were calculated using the intersect command in BEDTools (v2.28.0)[47] with default options. To normalize sequencing depth for each sample, we utilized bamCompare from deepTools (v3.3.0)[48] to generate a bigWig file based on two BAM files that are compared to each other. Finally, peaks were ordered by binding strength, and heat maps were plotted using deepTools[48].

Histone extraction and western blotting. Total lysates were obtained through lysing cells in RIPA buffer with protease inhibitors on ice for 30 min. For acid extraction, cells were lysed in hypotonic lysis buffer containing 10 mM HEPES, 10 mM KCl, 1.5 mM $MgCl_2$, 0.5 mM dithiothreitol and protease inhibitors. H_2SO_4 was then added to a final concentration of 0.2 M and incubated for 30 min at 4 °C. After spinning down, proteins in supernatants were precipitated in 33% trichloroacetic acid, washed with acetone and resuspended in ddH_2O. Protein extracts were quantified by BCA protein assay (Bio-Rad), and used for western blot analysis of acetylated histones and/or Ponceau S staining to visualize total histones. Western blots were quantified using ImageJ (v2.0.2).

Quantitative PCR analysis. RNA was isolated from cells in triplicate wells in each condition by using Trizol Reagent (Life Technologies, Invitrogen). Generally, 2 μg of RNA for each sample was reversed to cDNA by First-strand cDNA Synthesis System (Marligen Biosciences). All real-time PCR reactions were performed using the 7900HT Fast Real-Time PCR System (Applied Biosystem), and the amplifications were done using SYBR Green PCR Master Mix (Applied Biosystems). All experiments were performed in triplicate. The statistical analysis was performed by GraphPad Prism (v8.0). Gene expression levels were normalized to an internal control gene. qPCR primer sequences were: m*ME1*-F: TTCCTACGTGTTCCCTGGAG; m*ME1*-R: GGCCTTCTTGCAGGT GTTTA; m*ME2*-F: TTACCCGTCGCTGGCTAATA; m*ME2*-R: TGCTCCGCCATA TTCTCTCT; m*C/EBPα*-F: GCCGAGATAAAGCCAAACAAC; m*C/EBPα*-R: TCTCAGGCAGCTGGCGGAAG; m*PPARγ*-F: GAATGACCAAGTGACTC TGCTC; m*PPARγ*-R: GGTCATGAATCCTTGGCCC; m*Adipoq*-F: CTGTTGCA AGCTCTCCTGTTCC; m*Adipoq*-R: GGCCAGGATGTCCTGGGATGC; m*β-actin*-F: TACCACAGGCATTGTGATGGAC; m*β-actin*-R: ACGCTCGGTC AGGATCTTCATG; m*G6PD*-F: GCCACTCCAGAAGAAAGACCT; m*G6PD*-R: GGCAAGGCCAGGTAGAATAG; m*p53*-F: GAAGTCCTTTGCCCTGAAC; m*p53*-R: CTAGCAGTTTGGGCTTTCC; h*ME1*-F: GTGTGGATTGAGGC AGA; h*ME1*-R: GCGGTTCAGGATAAACTGT; h*ME2*-F: ATTAGTGACAGT GTTTTCCTA; h*ME2*-R: TCAGGTTCTGGGTATCG; h*β-actin*-F: TGACGTGG ACATCCGCAAAG; h*β-actin*-R: CTGGAAGGTGGACAGCGAGG; h*HDAC3*-F: CACCCGCATCGAGAATCAGA; h*HDAC3*-R: TGCAGGCACGTCATGAATCT; h*HK2*-F: GATGTGGCTGTGGATGAGCT; h*HK2*-R: AGATGCCCCTTGTCT TGAGC; h*PFK1*-F: CGCCAAGGCTATGAACTGGA; h*PFK1*-R: TGGAAGACC AGAGCCCTCTT; h*LDHA*-F: AGAATCTTAGGCGGGTGCAC; h*LDHA*-R: TTCA AACGGGCCTCTTCCTC; h*Got1*-F: CTGGGACCTGGAACCACATC; h*Got1*-R: CGTTGATTCGACCACTTGGC; h*ChREBP*-F: CGGCCTCTGTTTGAGTCCTT; h*ChREBP*-R: GCGTAGGGAGTTCAGGACAG; h*Glut4*-F: TCTCCAACTGGA CGAGCAAC; h*Glut4*-R: CAGCAGGAGGACCGCAAATA; h*GAPDH*-F: GGAGCGAGATCCCTCCAAAAT; h*GAPDH*-R: GGCTGTTGTCATACTTC TCATGG; m*FABP4*-F: AACGAGATGGTGACAAGCTG; m*FABP4*-R: AATTT CCATCCAGGCCTCTT; m*HDAC3*-F: TTGAAGATGCTGAACCATGC; and m*HDAC3*-R: TGGCCTGCTGTAGTTCTCCT.

Recombinant protein expression and purification. Mouse *Hdac3* gene (WT) was cloned from 3T3-L1 cells using RT–PCR. *HDAC3* was then cloned into prokaryotic GST-fused expression vector pGEX-6p-1 and PRK5–Flag. GST-tagged HDAC3 construct was transformed into *Escherichia coli* strain BL21 (DE3) and

1 mM isopropyl-β-D-thiogalactoside (IPTG) was added to induce recombinant protein expression overnight at 15 °C. Cells were harvested, resuspended in 50 ml lysis buffer containing 100 mM Tris-HCl (pH 8.0), 100 mM NaCl, 50 mM EDTA, 1% Triton X-100, 5 mM dithiothreitol and 1.67 mg ml^{-1} lysozyme for 30 min and sonicated. GST fusion proteins were affinity purified with GSH sepharose 4B and eluted with elution buffer (50 mM Tris-HCl (pH 8.0) and 10 mM GSH). Proteins were analysed by 12% SDS–PAGE with Coomassie blue staining. Flag–HDAC3 (WT) and its mutants (L1, L6 and R301A) were purified from HEK293T cells using 3× Flag peptide elution. Purified proteins were used for the GST pull-down assay or Biacore analysis.

Immunoprecipitation. For immunoprecipitation, cells were lysed in IP lysis buffer containing 50 mM Tris (pH 7.4), 150 mM NaCl, 1 mM EDTA, 1% NP-40 and protease inhibitors for 2 h. Anti-Flag M2 affinity gels were added to supernatants. After incubation, beads were washed five times with lysis buffer and boiled in 2× loading buffer and resolved by SDS–PAGE.

Measurements of NADPH, HDAC3 and HAT activities. NADPH levels were analysed by $NADP^+$/NADPH Quantification Kit (K347, BioVision), HDAC3 enzymatic activity was examined using HDAC3 activity assay kit (K343, BioVision), and HAT activity was analysed by HAT activity assay kit (ab65352, Abcam), following the manufacturers' instructions.

Measurements of $NADP^+$, NAD^+ and NADH. NAD^+ and NADH levels were analysed using NAD^+/NADH Quantification Kit (K337) and $NADP^+$ levels using assay kit K347 (all from BioVision), following the manufacturer's instructions.

Drug affinity responsive targets stability. DARTS was performed as described previously[49]. Briefly, 5×10^7 HEK293T cells were lysed in M-PER (78501, Thermo Fisher Scientific) with protease inhibitor cocktail and phosphatase inhibitor cocktail. Then, TNC buffer (50 mM Tris-HCL (pH 8.0), 50 mM NaCl and 10 mM $CaCl_2$) was added to the lysate, and the protein concentration was measured by BCA assay. Cell lysates were incubated with various concentrations of NAD^+, NADH, $NADP^+$, NADPH, Ins(1,4,5,6)P_4 or PBS (vehicle) for 1 h at RT and digested with pronase (1:3,000 dilution for HDAC3; 10165921001, Roche) for 30 min at RT. The digestion was stopped by protease inhibitor cocktail, and then the samples were immediately placed on ice. Finally, western blotting was used to determine whether HDAC3 is a direct target of NAD^+, NADH, $NADP^+$, NADPH or Ins(1,4,5,6)P_4. Tubulin was used as a negative control. Protein intensity was quantified through ImageJ software (v2.0.2).

Cellular thermal shift assay. CETSAs were performed to determine the direct binding between NAD^+, NADH, $NADP^+$, NADPH or Ins(1,4,5,6)P_4 and HDAC3 in cellular as described before[49]. Briefly, 4×10^6 HEK293T cells were pretreated with NAD^+, NADH, $NADP^+$, NADPH or Ins(1,4,5,6)P_4 for 12 h before being subjected to the CETSA protocol. Cells were chilled on ice, and then washed with PBS containing protease inhibitor cocktail. The cells were heat shocked at the indicated temperature for 3 min to denature proteins in the Bio-Rad T100 Thermal Cycler, and then immediately cooled at RT for 3 min.

Finally, all samples were frozen with dry ice and thawed with Thermal Cycler for three times to lyse cells, followed by centrifugation at 20,000*g* for 20 min at 4 °C. Then the supernatants were boiled with 4× Laemmli Sample Buffer (1610747, Bio-Rad) for western blotting. The bands were quantified using ImageJ (v2.0.2).

Surface plasmon resonance analysis of interactions. SPR analysis was carried out at 25 °C with a Biacore T200 biomolecular interaction analysis system (GE Healthcare) according to the manufacturer's instructions. Flag-tagged HDAC3 was immobilized on the surface of a CM5 sensor chip in 10 mM sodium acetate buffer (pH 4.5) and functioned as the stationary phase. As the mobile phase, NAD^+, NADH, $NADP^+$, NADPH or Ins(1,4,5,6)P_4 flowed through the sensor chip surface at different concentrations in a running buffer of PBS at a flow rate of 30 µl min^{-1}. After each cycle of binding and dissociation, the surface was regenerated with 10 mM glycine (pH 2.0). The affinity parameters were analysed by Biacore T200 evaluation software.

Molecular docking. The docking studies were performed by AutoDock Vina (v1.1.2). NADPH structure was taken from the crystal structure under Protein Data Bank (PDB) ID 5AQ1 followed by an energy-minimization step using Amber16 (ref. [50]), while Ins(1,4,5,6)P_4 was taken from the crystal structure under PDB ID 4A69 and was used without this step. The chain A of this crystal structure (HDAC3) was chosen as the receptor. Both ligand and receptor were processed with Autodock Tools for the preparation of docking, and all the rotatable bonds in the ligand were allowed to be rotated during docking. For the objective docking, the grid size was set to 40×40×52 points with a grid spacing of 1 Å around the centre of a potential binding pocket involving H17, G21, K25, R265, L266 and R301. Nine independent docking runs were carried out for each ligand. The resultant docking poses were analysed and visualized by PyMOL (v1.8). To calculate the root mean squared deviation of Ins(1,4,5,6)P_4 between the native pose as seen in the crystal structure and the predicted pose from AutoDock Vina, the coordinates of all heavy atoms were compared in the pairwise manner except for three oxygen atoms in each phosphate group whose rotameric states would have complicated the calculation.

Molecular dynamics simulations. Structural models of HDAC3, HDAC3–DAD and Ins(1,4,5,6)P_4 were taken from the crystal structure under PDB ID 4A69 or docked structures by AutoDock Vina. Simulations were performed using the GPU-accelerated PMEMD programme in AMBER 18 package with ff14SB force-field parameters[51]. The force-field parameters of NADPH were extracted from a previously published paper[52], while GAFF parameters[53] were used for Ins(1,4,5,6)P_4. The zinc metal centre was set up following a previous study[39]. The initial structure was solvated in a truncated octahedral water box with the SPC/E water model. The size of the water box was chosen such that the boundary of the box was at least 10 Å away from any of the protein atoms. Sodium and chloride ions were added into the water box to mimic the experimental salt concentration (0.15 M) and to neutralize the system according to the Coulombic potential distribution. The resulting water box was then subjected to energy minimization for 1,000 steps using harmonic restraints with force constant of 500 kcal mol^{-1} $Å^{-2}$, followed by 1,000 steps of unrestrained minimization. The optimized system was heated from 0 to 298 K and then equilibrated at 298 K for 1 ns using the isothermal–isobaric (NPT) ensemble. Finally, a trajectory was recorded for 500 ns at 298 K under the NPT ensemble. The integration time step was set to 2 fs, and the non-bonded cut-off was set to 8 Å.

Statistics and reproducibility. Statistical parameters including the exact sample sizes, *P* values and error bars are defined in the figures and corresponding legends. Unless otherwise stated, all figures are representative of at least three independent experiments. For immunoblotting results and Oil Red O staining, we show representative data from at least three replicates. For the immunoblotting of proteins in similar molecular weights, samples derived from the same experiments and gels were processed in parallel. For CHIP–seq analysis, there were no technical replicates for anti-Ac-H2B or Ac-H3 CHIP–seq, and two technical replicates for anti-HDAC3 CHIP–seq.

Statistical analyses and graphing were performed using GraphPad Prism (v.8.0). To assess statistical significance, comparisons between two groups were performed using an unpaired, two-tailed Student's *t*-test. Results are presented as the mean ± s.d. *P* values < 0.05 were considered to be statistically significant.

Reporting Summary. Further information on research design is available in the Nature Research Reporting Summary linked to this article.

Data availability

Uncropped versions of blots and source data are provided with this paper. The CHIP–seq data have been deposited in the Gene Expression Omnibus under accession GSE137694. The remaining data that support the findings of this study are available from the corresponding author upon reasonable request.

Received: 3 September 2019; Accepted: 10 December 2020;
Published online: 18 January 2021

References

1. Lunt, S. Y. & Vander Heiden, M. G. Aerobic glycolysis: meeting the metabolic requirements of cell proliferation. *Annu. Rev. Cell Dev. Biol.* **27**, 441–464 (2011).
2. Vander Heiden, M. G., Cantley, L. C. & Thompson, C. B. Understanding the Warburg effect: the metabolic requirements of cell proliferation. *Science* **324**, 1029–1033 (2009).
3. Du, W. et al. TAp73 enhances the pentose phosphate pathway and supports cell proliferation. *Nat. Cell Biol.* **15**, 991–1000 (2013).
4. Fan, J. et al. Quantitative flux analysis reveals folate-dependent NADPH production. *Nature* **510**, 298–302 (2014).
5. Jeon, S. M., Chandel, N. S. & Hay, N. AMPK regulates NADPH homeostasis to promote tumour cell survival during energy stress. *Nature* **485**, 661–665 (2012).
6. Jiang, P., Du, W., Mancuso, A., Wellen, K. E. & Yang, X. Reciprocal regulation of p53 and malic enzymes modulates metabolism and senescence. *Nature* **493**, 689–693 (2013).
7. Liu, L. et al. Malic enzyme tracers reveal hypoxia-induced switch in adipocyte NADPH pathway usage. *Nat. Chem. Biol.* **12**, 345–352 (2016).
8. Jiang, P. et al. p53 regulates biosynthesis through direct inactivation of glucose-6- phosphate dehydrogenase. *Nat. Cell Biol.* **13**, 310–316 (2011).
9. Kinnaird, A., Zhao, S., Wellen, K. E. & Michelakis, E. D. Metabolic control of epigenetics in cancer. *Nat. Rev. Cancer* **16**, 694–707 (2016).
10. Comerford, S. A. et al. Acetate dependence of tumors. *Cell* **159**, 1591–1602 (2014).
11. Montgomery, D. C., Sorum, A. W., Guasch, L., Nicklaus, M. C. & Meier, J. L. Metabolic regulation of histone acetyltransferases by endogenous Acyl-CoA cofactors. *Chem. Biol.* **22**, 1030–1039 (2015).
12. Su, X., Wellen, K. E. & Rabinowitz, J. D. Metabolic control of methylation and acetylation. *Curr. Opin. Chem. Biol.* **30**, 52–60 (2016).

13. Takahashi, H., McCaffery, J. M., Irizarry, R. A. & Boeke, J. D. Nucleocytosolic acetyl-coenzyme a synthetase is required for histone acetylation and global transcription. *Mol. Cell* **23**, 207–217 (2006).
14. Wellen, K. E. et al. ATP-citrate lyase links cellular metabolism to histone acetylation. *Science* **324**, 1076–1080 (2009).
15. Cohen, H. Y. et al. Calorie restriction promotes mammalian cell survival by inducing the SIRT1 deacetylase. *Science* **305**, 390–392 (2004).
16. Imai, S., Armstrong, C. M., Kaeberlein, M. & Guarente, L. Transcriptional silencing and longevity protein Sir2 is an NAD-dependent histone deacetylase. *Nature* **403**, 795–800 (2000).
17. Lu, C. & Thompson, C. B. Metabolic regulation of epigenetics. *Cell Metab.* **16**, 9–17 (2012).
18. Yang, H. et al. Nutrient-sensitive mitochondrial NAD^+ levels dictate cell survival. *Cell* **130**, 1095–1107 (2007).
19. Perissi, V., Jepsen, K., Glass, C. K. & Rosenfeld, M. G. Deconstructing repression: evolving models of co-repressor action. *Nat. Rev. Genet.* **11**, 109–123 (2010).
20. Sun, Z. et al. Deacetylase-independent function of HDAC3 in transcription and metabolism requires nuclear receptor corepressor. *Mol. Cell* **52**, 769–782 (2013).
21. Guenther, M. G., Barak, O. & Lazar, M. A. The SMRT and N-CoR corepressors are activating cofactors for histone deacetylase 3. *Mol. Cell. Biol.* **21**, 6091–6101 (2001).
22. Watson, P. J., Fairall, L., Santos, G. M. & Schwabe, J. W. Structure of HDAC3 bound to co- repressor and inositol tetraphosphate. *Nature* **481**, 335–340 (2012).
23. Rubin, C. S., Hirsch, A., Fung, C. & Rosen, O. M. Development of hormone receptors and hormonal responsiveness in vitro. Insulin receptors and insulin sensitivity in the preadipocyte and adipocyte forms of 3T3-L1 cells. *J. Biol. Chem.* **253**, 7570–7578 (1978).
24. Cristancho, A. G. & Lazar, M. A. Forming functional fat: a growing understanding of adipocyte differentiation. *Nat. Rev. Mol. Cell Biol.* **12**, 722–734 (2011).
25. Molchadsky, A. et al. p53 is required for brown adipogenic differentiation and has a protective role against diet-induced obesity. *Cell Death Differ.* **20**, 774–783 (2013).
26. Yoo, E. J., Chung, J. J., Choe, S. S., Kim, K. H. & Kim, J. B. Down-regulation of histone deacetylases stimulates adipocyte differentiation. *J. Biol. Chem.* **281**, 6608–6615 (2006).
27. Johnsson, A., Xue-Franzen, Y., Lundin, M. & Wright, A. P. H. Stress-specific role of fission yeast Gcn5 histone acetyltransferase in programming a subset of stress response genes. *Eukaryot. Cell* **5**, 1337–1346 (2006).
28. Menzies, K. J., Zhang, H., Katsyuba, E. & Auwerx, J. Protein acetylation in metabolism—metabolites and cofactors. *Nat. Rev. Endocrinol.* **12**, 43–60 (2016).
29. Shi, L. & Tu, B. P. Acetyl-CoA and the regulation of metabolism: mechanisms and consequences. *Curr. Opin. Cell Biol.* **33**, 125–131 (2015).
30. Wood, M., Rymarchyk, S., Zheng, S. & Cen, Y. Trichostatin A inhibits deacetylation of histone H3 and p53 by SIRT6. *Arch. Biochem. Biophys.* **638**, 8–17 (2018).
31. Yoshida, M. Potent and specific inhibition of mammalian histone deacetylase both in vivo and in vitro by trichostatin A. *Tanpakushitsu Kakusan Koso* **52**, 1788–1789 (2007).
32. Saito, A. et al. A synthetic inhibitor of histone deacetylase, MS-27-275, with marked in vivo antitumor activity against human tumors. *Proc. Natl Acad. Sci. USA* **96**, 4592–4597 (1999).
33. Li, Z. Y. et al. Histone deacetylase inhibitor RGFP109 overcomes temozolomide resistance by blocking NF-κB-dependent transcription in glioblastoma cell lines. *Neurochem. Res.* **41**, 3192–3205 (2016).
34. Hideshima, T. et al. Discovery of selective small-molecule HDAC6 inhibitor for overcoming proteasome inhibitor resistance in multiple myeloma. *Proc. Natl. Acad. Sci. USA* **113**, 13162–13167 (2016).
35. Marek, L. et al. Histone deacetylase (HDAC) inhibitors with a novel connecting unit linker region reveal a selectivity profile for HDAC4 and HDAC5 with improved activity against chemoresistant cancer cells. *J. Med. Chem.* **56**, 427–436 (2013).
36. Malvaez, M. et al. HDAC3-selective inhibitor enhances extinction of cocaine-seeking behavior in a persistent manner. *Proc. Natl Acad. Sci. USA* **110**, 2647–2652 (2013).
37. Cracan, V., Titov, D. V., Shen, H., Grabarek, Z. & Mootha, V. K. A genetically encoded tool for manipulation of $NADP^+$/NADPH in living cells. *Nat. Chem. Biol.* **13**, 1088–1095 (2017).
38. Trott, O. & Olson, A. J. AutoDock Vina: improving the speed and accuracy of docking with a new scoring function, efficient optimization and multithreading. *J. Comput. Chem.* **31**, 455–461 (2010).
39. Arrar, M., Turnham, R., Pierce, L., de Oliveira, C. A. & McCammon, J. A. Structural insight into the separate roles of inositol tetraphosphate and deacetylase-activating domain in activation of histone deacetylase 3. *Protein Sci.* **22**, 83–92 (2013).
40. Vogelauer, M., Krall, A. S., McBrian, M. A., Li, J. Y. & Kurdistani, S. K. Stimulation of histone deacetylase activity by metabolites of intermediary metabolism. *J. Biol. Chem.* **287**, 32006–32016 (2012).
41. Alenghat, T. et al. Nuclear receptor corepressor and histone deacetylase 3 govern circadian metabolic physiology. *Nature* **456**, 997–1000 (2008).
42. Feng, L. et al. Nonreciprocal light propagation in a silicon photonic circuit. *Science* **333**, 729–733 (2011).
43. Rey, G. et al. The pentose phosphate pathway regulates the circadian clock. *Cell Metab.* **24**, 462–473 (2016).
44. Li, H. & Durbin, R. Fast and accurate short read alignment with Burrows–Wheeler transform. *Bioinformatics* **25**, 1754–1760 (2009).
45. Li, H. et al. The Sequence Alignment/Map format and SAMtools. *Bioinformatics* **25**, 2078–2079 (2009).
46. Zhang, Y. et al. Model-based analysis of ChIP–seq (MACS). *Genome Biol.* **9**, R137 (2008).
47. Quinlan, A. R. & Hall, I. M. BEDTools: a flexible suite of utilities for comparing genomic features. *Bioinformatics* **26**, 841–842 (2010).
48. Ramirez, F. et al. deepTools2: a next generation web server for deep-sequencing data analysis. *Nucleic Acids Res.* **44**, W160–W165 (2016).
49. Su, R. et al. R-2HG exhibits anti-tumor activity by targeting FTO/m^6A/MYC/CEBPA signaling. *Cell* **172**, 90–105 (2018).
50. Case, D. A. et al. The amber biomolecular simulation programs. *J. Comput. Chem.* **26**, 1668–1688 (2005).
51. Maier, J. A. et al. ff14SB: improving the accuracy of protein side chain and backbone parameters from ff99SB. *J. Chem. Theory Comput.* **11**, 3696–3713 (2015).
52. Holmberg, N., Ryde, U. & Bulow, L. Redesign of the coenzyme specificity in L-lactate dehydrogenase from bacillus stearothermophilus using site-directed mutagenesis and media engineering. *Protein Eng.* **12**, 851–856 (1999).
53. Wang, J., Wolf, R. M., Caldwell, J. W., Kollman, P. A. & Case, D. A. Development and testing of a general amber force field. *J. Comput. Chem.* **25**, 1157–1174 (2004).

Acknowledgements

We thank X. Wang and H. Liu for helping with analysis of ChIP–seq data. This work was supported by the National Key Research and Development Program of China (2019YFA0802600), CAMS Innovation Fund for Medical Sciences (2016-I2M-4-002), the National Natural Science Foundation of China (81672766), State Key Laboratory Special Fund (2060204), CAMS Basic Research Fund (2019-RC-HL-007, 2016ZX310186 and 2016RC310038) to W.D. and a postdoctoral fellowship at Peking-Tsinghua Center for Life Sciences and National Science Foundation for Young Scholars of China (31601154) and China Postdoctoral Science Foundation (2016M601005; to J.Q.)

Author contributions

W.L., J.K. and J.Q. performed all experiments except those mentioned below. Y.P. and Y.X. performed the molecular docking calculation and MD simulations and interpreted the data. L.L. and Z.Z. helped with animal experiments. W.D. designed the experiments. W.D. and W.L. analysed the data. W.D. wrote the manuscript with the help of Y.X. All authors discussed the results and commented on the manuscript.

Competing interests

The authors declare no competing interests.

Additional information

Extended data is available for this paper at https://doi.org/10.1038/s42255-020-00330-2.

Supplementary information is available for this paper at https://doi.org/10.1038/s42255-020-00330-2.

Correspondence and requests for materials should be addressed to Y.X. or W.D.

Peer review information Primary Handling Editor: Christoph Schmitt. *Nature Metabolism* thanks Michael Parker and the other, anonymous, reviewer(s) for their contribution to the peer review of this work.

Reprints and permissions information is available at www.nature.com/reprints.

Publisher's note Springer Nature remains neutral with regard to jurisdictional claims in published maps and institutional affiliations.

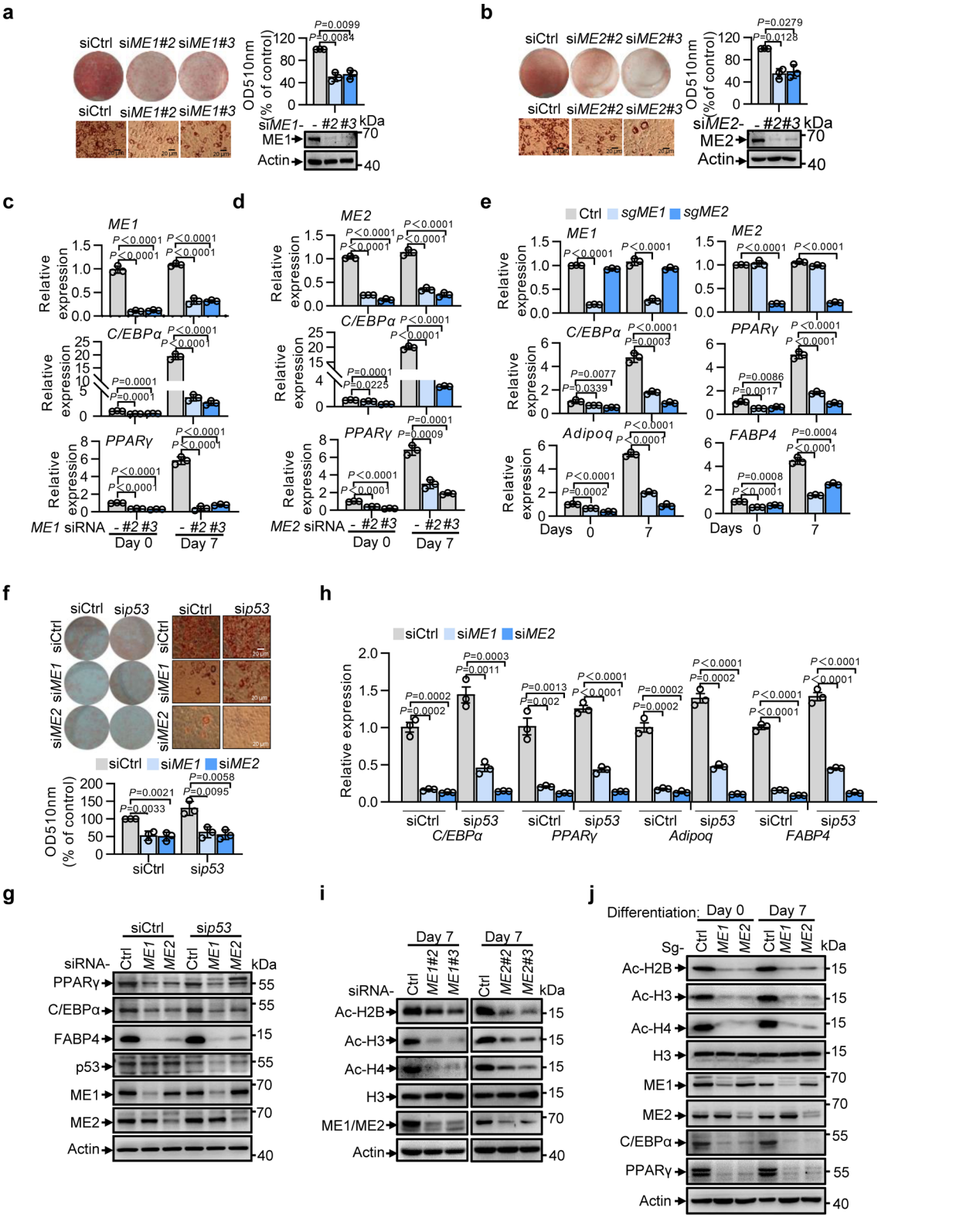

Extended Data Fig. 1 | See next page for caption.

Extended Data Fig. 1 | ME silencing impairs adipocyte differentiation, histone acetylation and genes transcription. a, b, 3T3-L1 preadipocytes transfected with control siRNA, or different sets of *ME1* (**a**) or *ME2* siRNAs (**b**) as indicated were induced to differentiate for 7 days. The accumulation of differentiation-induced lipid droplets was visualized by Oil Red O staining (left). Oil Red O staining was quantified (right, top panel). The protein expression is shown below. **c**, **d**, mRNA expression of 3T3-L1 preadipocytes transfected with control siRNA, or different sets of *ME1* (**c**) or *ME2* siRNAs (**d**) as indicated before (Day 0) and after differentiating for 7 days (Day 7). **e**, mRNA expression of control or *ME* knockout 3T3-L1 cells using sgRNA CRISPR/Cas9. **f**–**h**, 3T3-L1 preadipocytes transfected with control, *ME1*, *ME2* and/or *p53* siRNAs as indicated were induced to differentiate for 7 days. Cells were stained with Oil Red O (**f**, top). Oil Red O staining was quantified (**f**, bottom). Protein expression (**g**) and mRNA levels (**h**) are shown. **i**, Western blots of 3T3-L1 preadipocytes transfected with control siRNA, or different sets of *ME1* (left) or *ME2* siRNAs (right) as indicated after 7 days of differentiation. **j**, Protein expression of control or *ME* knockout 3T3-L1 cells using sgRNA CRISPR/Cas9 after differentiating for 7 days. In **a, b, f**, n = 3 biological replicates; In **c, d, e, h**, n = 3 technical replicates of one out of three independent experiments with similar results. Data are mean ± s.d. Statistical significance was determined by two-tailed unpaired *t*-test. In **a**, **b**, **f**, **g**, **i**, **j**, Oil Red O staining images and western blots represent three independent experiments. For all western blot data, histone expression was analyzed using acid-extracted cell lysates, total H3 was used as loading control; all other protein expression was assessed with total cell lysates, Actin was used as loading control. The samples derived from the same experiment and the blots were processed in parallel.

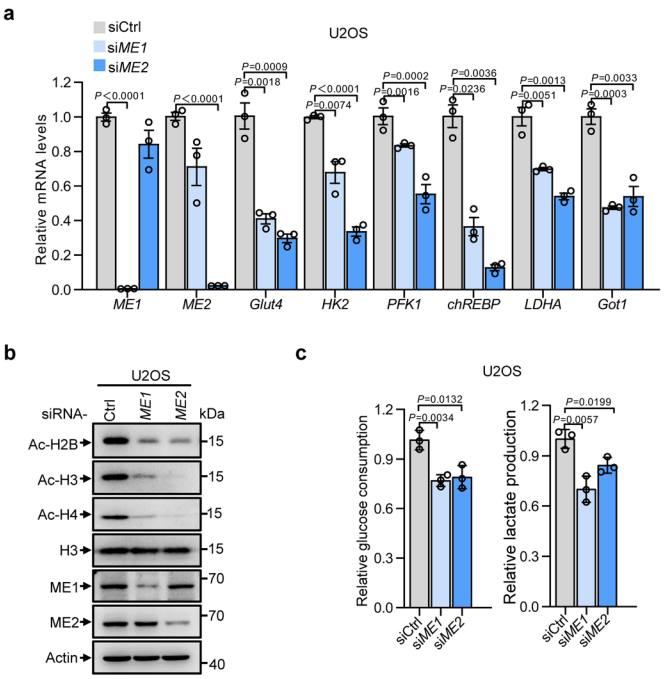

Extended Data Fig. 2 | MEs inhibition resulted in decreased histone acetylation and glycolytic genes expression. U2OS cells were transfected with control, *ME1* or *ME2* siRNA for 48 hours. **a**, RNA was extracted and expressions of glucose metabolism genes were analyzed by qRT-PCR. **b**, Acid extracts were analyzed by western blot with antibodies against indicated acetylated histones. Expressions of actin and total H3 were determined as loading controls. Western blots represent three independent experiments. **c**, Relative glucose consumption and lactate production were determined by YSI2700 Biochemistry Analyzer. In **a**, n = 3 technical replicates of one out of three independent experiments with similar results; In **c**, n = 3 biological replicates. Data are mean ± s.d.. Statistical significance was determined by two-tailed unpaired *t*-test.

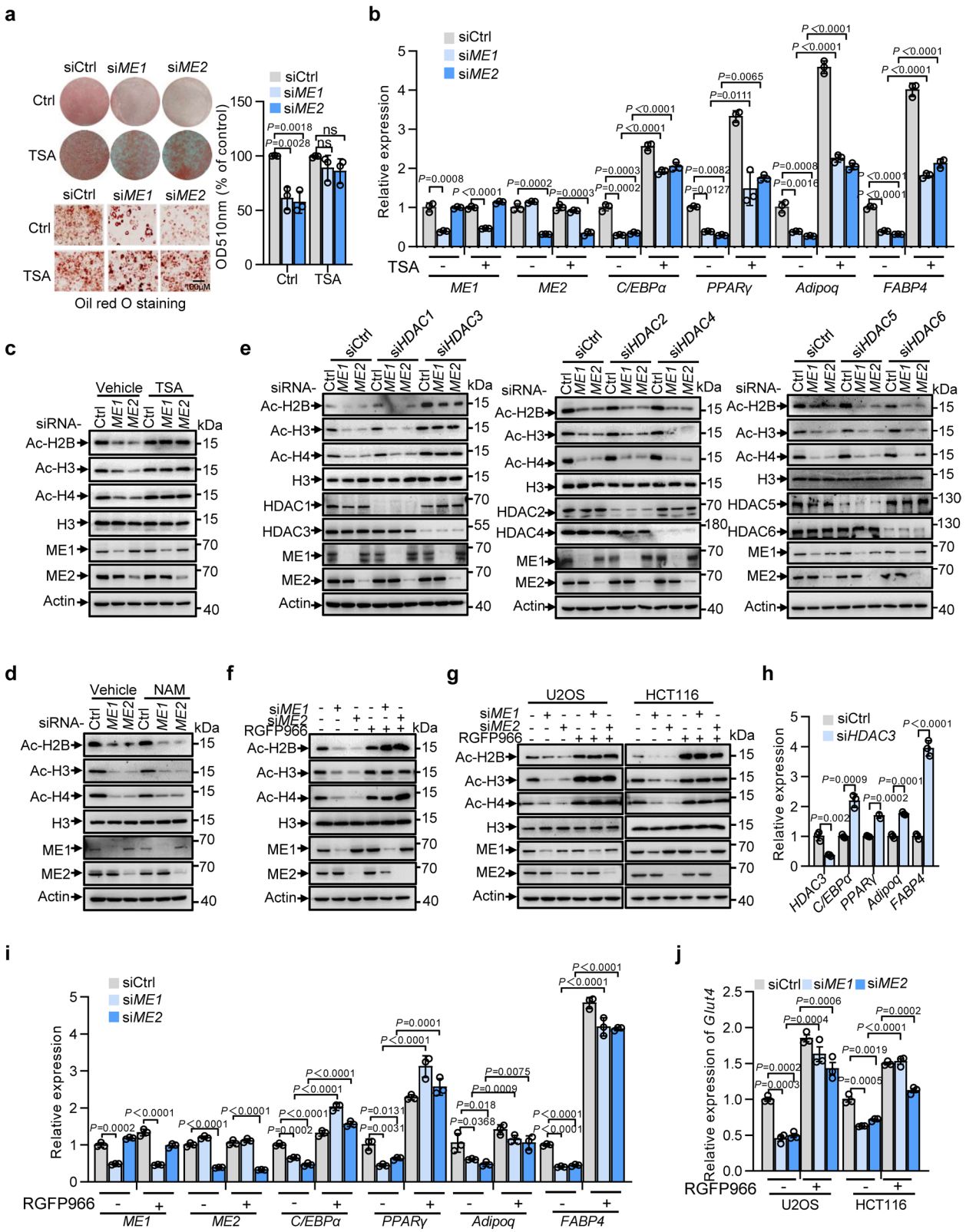

Extended Data Fig. 3 | See next page for caption.

Extended Data Fig. 3 | HDAC3 mediates ME-regulated histone acetylation and genes expression in adipocytes and tumour cells. a–c, 3T3-L1 preadipocytes transfected with control, *ME1* or *ME2* siRNA were induced to differentiate for 7 days with or without 0.1 μM TSA. (**a**) Cells were fixed and stained with Oil Red O (left). Oil Red O staining was quantified (right). (**b**) Relative gene expression was assessed by qRT-PCR. (**c**) Protein expression was analyzed by western blotting with specific antibodies. **d**, 3T3-L1 preadipocytes treated with control, *ME1* or *ME2* siRNA were induced to differentiate for 7 days in the absence or presence of 50 μM NAM. Protein expression was analyzed by western blot. **e**, Protein expression of U2OS cells transfected with control, *ME1* or *ME2* siRNA in presence of *HDAC1-6* siRNAs respectively as indicated. **f, i**, 3T3-L1 preadipocytes treated with control (−), *ME1* or *ME2* siRNA were induced to differentiate for 7 days with or without 10 μM RGFP966. Protein expression (**f**) and mRNA levels (**i**) are shown. **g, j**, U2OS and HCT116 cells were transfected with control (−), *ME1* or *ME2* siRNA and 2 days later treated with 10 μM RGFP966 for another 24 hours. Protein expression (**g**) and relative *Glut4* expression (**j**) are shown. **h**, 3T3-L1 preadipocytes transfected with control or *HDAC3* siRNAs were induced to differentiate for 7 days. Relative mRNA expression was assessed by qRT-PCR. In **a**, n = 3 biological replicates; In **b, h, i, j**, n = 3 technical replicates of one out of three independent experiments with similar results. Data are mean ± s.d.. Statistical significance was determined by two-tailed unpaired *t*-test. NS, not significant. In **a**, **c**, **d**, **e**, **f**, **g**, Oil Red O staining images and western blots represent three independent experiments. For all western blot data, histone expression was analyzed using acid-extracted cell lysates, total H3 was used as loading control; all other protein expression was assessed with total cell lysates, Actin was used as loading control. The samples derived from the same experiment and the blots were processed in parallel.

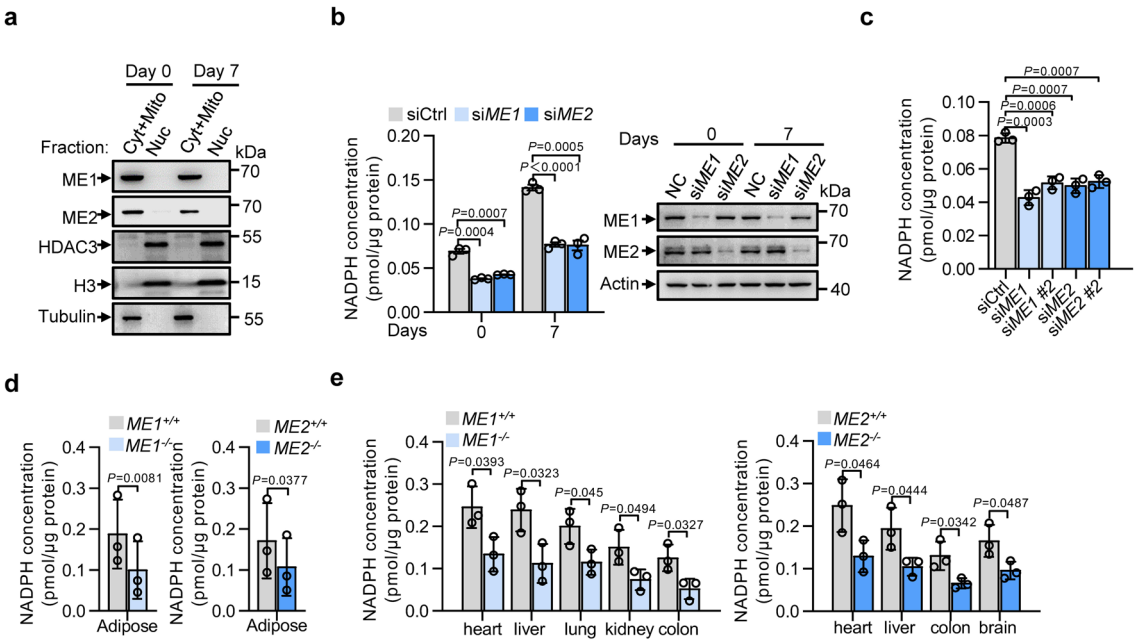

Extended Data Fig. 4 | Malic enzymes affect cellular NADPH levels. a, 3T3-L1 preadipocytes were induced to differentiate for 7 days. Before (day 0) and after differentiation induction (day 7), cells were fractionated and cytoplasmic (including mitochondria) and nuclear protein extracts were analyzed by western blot using indicated antibodies. Tubulin and total H3 were used as fraction and loading controls. Western blots represent three independent experiments. **b**, 3T3-L1 preadipocytes transfected with control, *ME1* or *ME2* siRNA were stimulated to differentiate for 7 days. Cellular NADPH levels were determined. Protein expression was determined by western blot. Actin was used as loading control. Western blots represent three independent experiments. **c**, Related to Figure. 2a and 2c. 3T3-L1 preadipocytes transfected with control siRNA, or two sets of *ME1* or *ME2* siRNAs as indicated, NADPH levels were determined. **d**, Adipose tissues from *ME1* or *ME2* knock-out mice (n = 3) were prepared for assaying NADPH levels. **e**, Tissues from *ME1* or *ME2* knock-out mice (n = 3) were analyzed NADPH levels using NADPH quantification kit. In **b, c, d, e**, n = 3 biological replicates; Data are mean ± s.d.. Statistical significance was determined by two-tailed unpaired *t*-test.

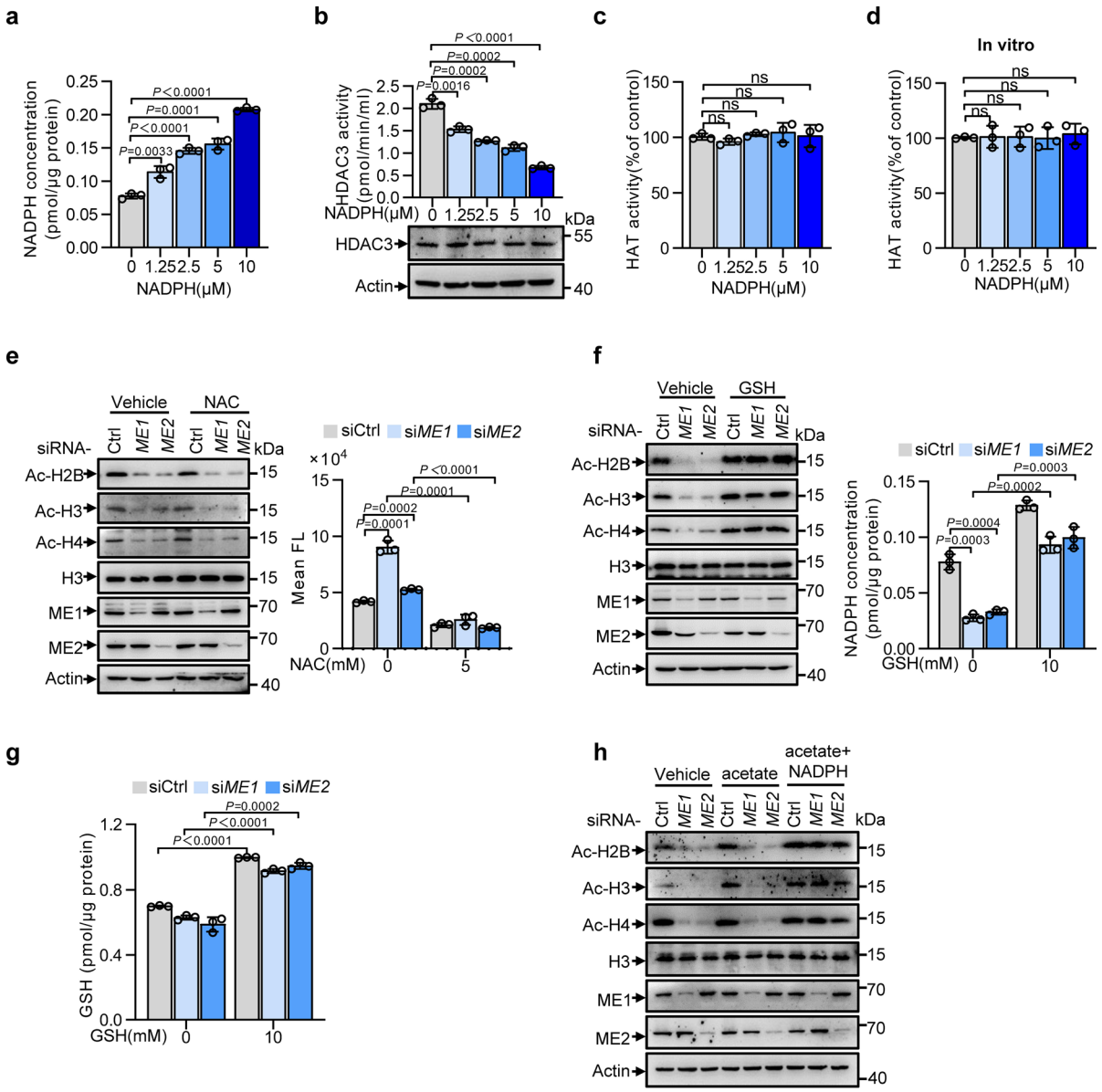

Extended Data Fig. 5 | NADPH is an endogenous inhibitor of HDAC3, ROS and acetyl-CoA are not involved in ME-mediated histone acetylation modification. a–c, 3T3-L1 preadipocytes were transfected with increased amount of NADPH using X-tremeGENE HP DNA Transfection reagent for 24h. (**a**) Cellular NADPH levels were examined. **b**, Cellular HDAC3 enzymatic activity were analyzed. HDAC3 expression were detected by western blotting. Actin was used as loading control. **c**, HAT activity of nucleic extracts was examined. **d**, Nucleic extracts from 3T3-L1 preadipocytes were incubated with increased amount of NADPH as indicated for 6h, and then HAT activity were determined. **e**, 3T3-L1 preadipocytes transfected with control (–), *ME1* or *ME2* siRNA were induced to differentiate for 7 days in the absence or presence of 5 mM NAC (N-acetyl-L-cysteine). Protein expression is shown (left). Cellular ROS levels were detected by FACS with DCF (2,7-dichlorodihydrofluorescein diacetate) staining (right). **f, g**, 3T3-L1 preadipocytes transfected with control (–), *ME1* or *ME2* siRNA were induced to differentiate for 7 days in the absence or presence of 10mM GSH as indicated. NADPH levels (**f** right panel) and GSH levels (**g**) were determined before differentiation (with 10mM GSH for 48h). Protein expression (**f** left panel) was analyzed after differentiation. **h**, 3T3-L1 preadipocytes transfected with control (–), *ME1* or *ME2* siRNA were induced to differentiate for 7 days in the absence or presence of 5 mM acetate combined with or without 10 μM NADPH as indicated. Protein expression was determined using western blot. In **a**, **b, c, d, e, f, g**, n = 3 biological replicates. Data are mean ± s.d.. Statistical significance was determined by two-tailed unpaired *t*-test. NS, not significant. For **b** (bottom panel), **e** (left panel), **f** (left panel), **h**, western blots represent three independent experiments. Histone expression was analyzed using acid-extracted cell lysates, total H3 was used as loading control; all other protein expression was assessed with total cell lysates, Actin was used as loading control. The samples derived from the same experiment and the blots were processed in parallel.

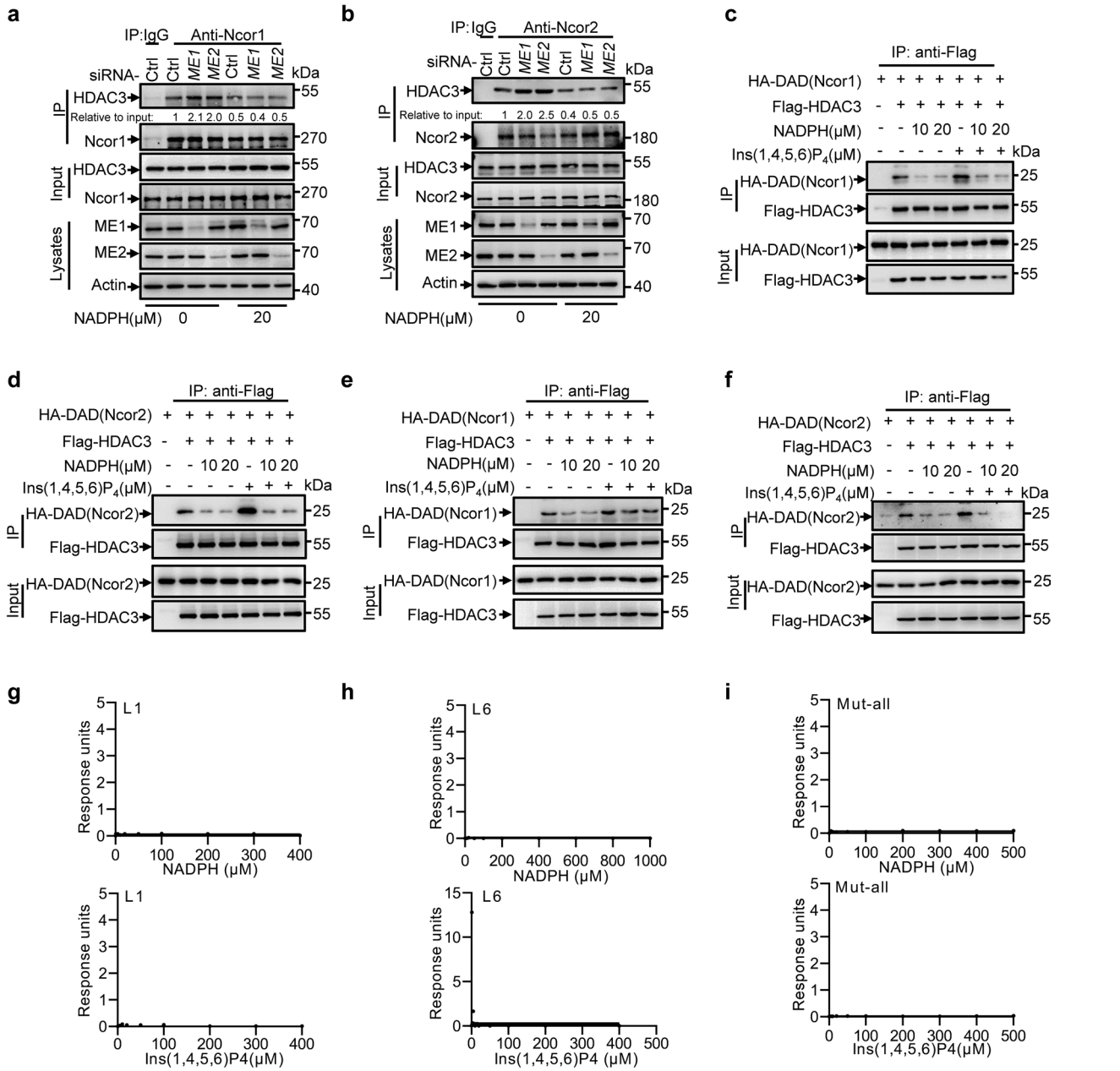

Extended Data Fig. 6 | NADPH disrupts HDAC3-DAD association. a, b, 3T3-L1 preadipocytes transfected with control, *ME1* or *ME2* siRNA as indicated were induced to differentiate for 7 days in the absence or presence of 20 μM NADPH (NADPH were transfected into cells using X-tremeGENE HP DNA Transfection reagent). Cells were then lysed and subjected to immunoprecipitation using anti-Ncor1 (**a**) or anti-Ncor2 (**b**) antibody. Input and bound proteins were analyzed by western blot. Actin was used as loading control. **c**, **d**, HA-DAD (Ncor1) (**c**), HA-DAD (Ncor2) (**d**) or Flag-HDAC3 was expressed in HEK293T cells individually. After 48 h, protein extracts from HA-DAD (Ncor1) (**c**) / HA-DAD (Ncor2) (**d**) and Flag-HDAC3 transfected cells were mixed at a ratio of 1:1 (Ncor1/Ncor2:HDAC3) in the presence or absence of NADPH and/or 20μM Ins(1,4,5,6)P4 (overnight) before immunoprecipitation using anti-IgG or anti-Flag antibody. **e**, **f**, HEK293T cells co-transfected with Flag-HDAC3 and HA-DAD(Ncor1) (**e**) or HA-DAD (Ncor2) (**f**) were treated with NADPH (NADPH were transfected into cells using X-tremeGENE HP DNA Transfection reagent) and/or Ins(1,4,5,6)P4 overnight as indicated. Cells were then lysed and subjected to immunoprecipitation using anti-Flag antibody. **g**–**i**, The dissociation constant (K_D) for immobilized mutant HDAC3 (L1, L6 or Mut-all) from NADPH or Ins(1,4,5,6)P4 were determined by surface plasmon resonance (SPR). Shown are real-time graphs of response units against NADPH or Ins(1,4,5,6)P4 concentrations. In **a**–**f**, western blots represent three independent experiments. The samples derived from the same experiment and the blots were processed in parallel.

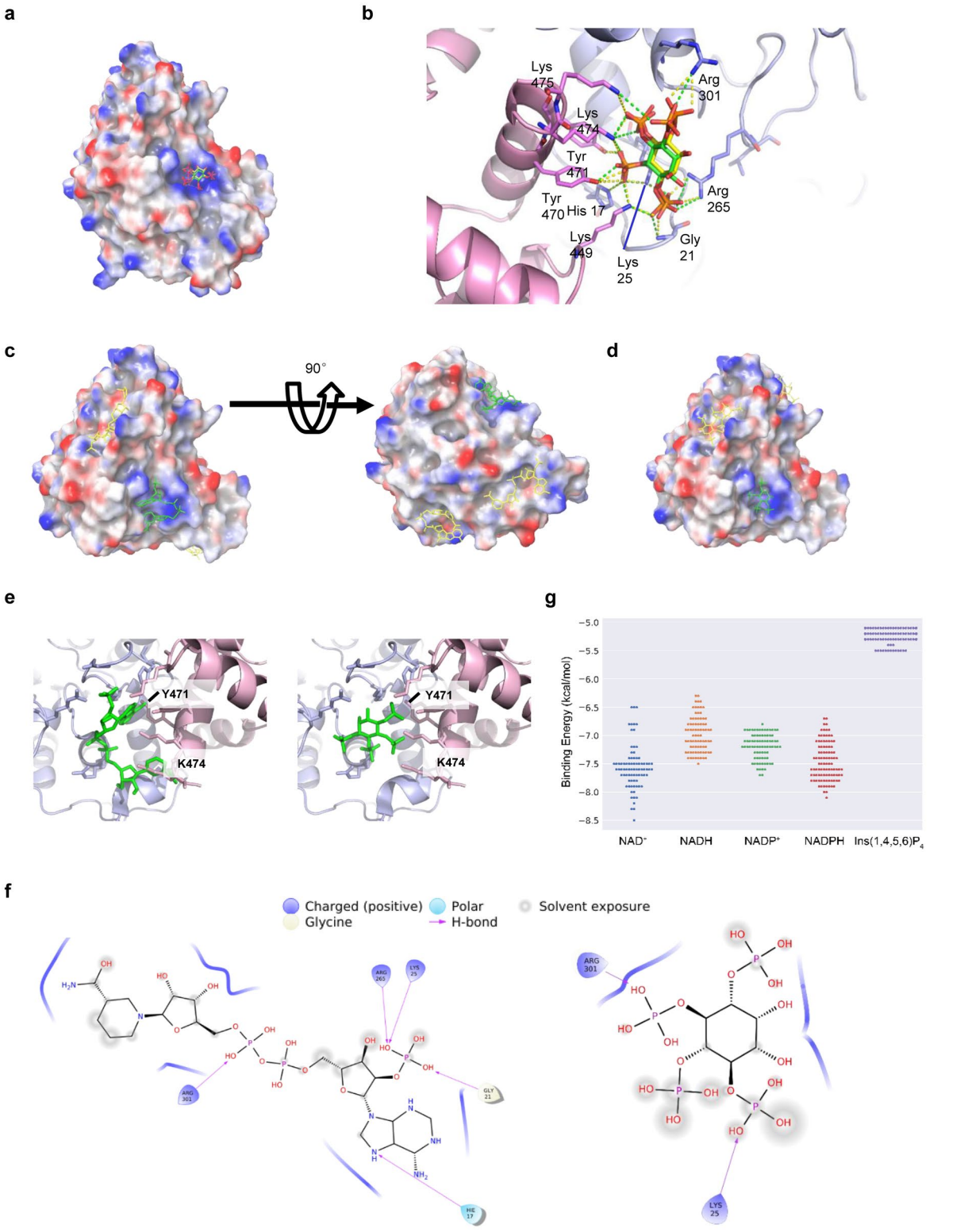

Extended Data Fig. 7 | See next page for caption.

Extended Data Fig. 7 | The molecular docking result targeting HDAC3. a, Electrostatic surface representation of the HDAC3-DAD complex onto which Ins(1,4,5,6)P4 docks. Ins(1,4,5,6)P4 molecules are shown in stick view either in green (the most energetically favored docking pose in the binding pocket) or in yellow (extracted from the crystal structure with PDB ID 4A69). **b**, The zoom-in structure of (a) showing details of the interaction between HDAC3-DAD complex and docked (green sticks) or native (yellow sticks) pose of Ins(1,4,5,6)P4. Hydrogen bonds and salt bridges are indicated by green or yellow dashed lines, respectively. HDAC3 (light blue) and DAD (magenta) are represented in cartoon view. **c**, The blind docking result of NADPH onto HDAC3. The pose in the binding interface is colored in green, other representative poses are colored in yellow. **d**, The blind docking result of Ins(1,4,5,6)P4 onto HDAC3. The pose in the binding interface is colored in green, other representative poses are colored in yellow. **e**, Clashes are found after adding DAD (magenta cartoon) into the docked structure of HDAC3-NADPH (left), while no clashes are observed when DAD is added into the docked structure of HDAC3-Ins(1,4,5,6)P4 (right). Residues from HDAC3-DAD binding interface are shown in sticks, clashed residues are highlighted by red circles. **f**, The 2D interaction diagrams are shown for the docking results of HDAC3-NADPH (left) and HDAC3-Ins(1,4,5,6)P4 (right). **g**, Statistics of binding energies for the docking results of NAD^+, NADH, $NADP^+$, NADPH and Ins(1,4,5,6)P4 targeting HDAC3. The objective docking was repeated for nine times, yielding 81 poses for each ligand.

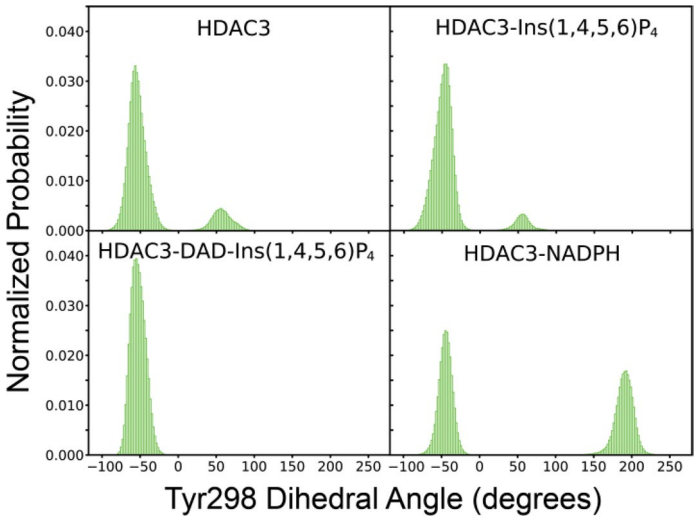

Extended Data Fig. 8 | The sidechain dynamics of Tyr 298 as revealed by MD simulations. The dihedral angle (N-C_α-C_β-C_γ) probability distributions of Tyr298 shown for MD simulations of HDAC3, HDAC3-Ins(1,4,5,6)P4, HDAC3-DAD-Ins(1,4,5,6)P4 and HDAC3-NADPH.

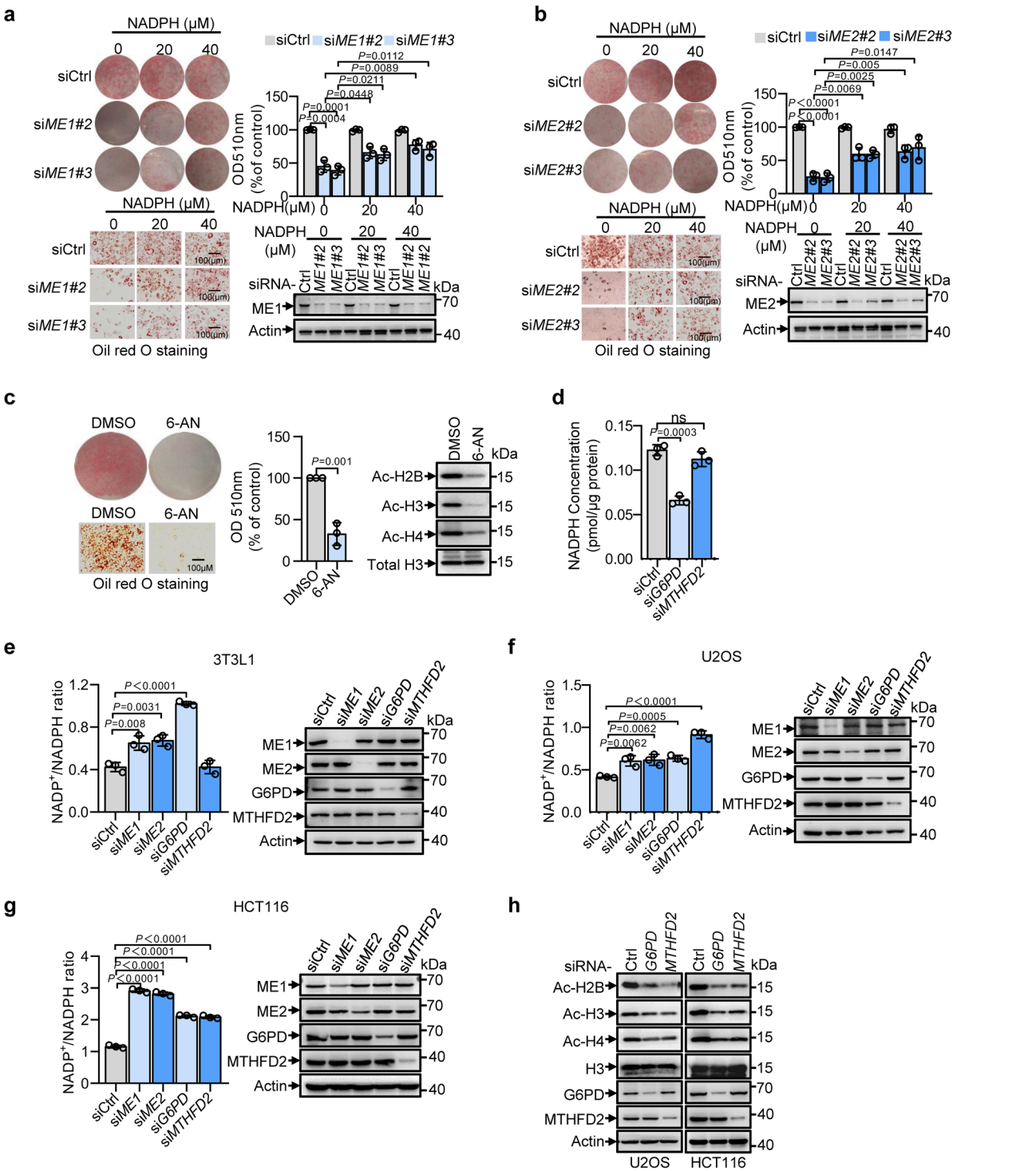

Extended Data Fig. 9 | NADPH promotes adipocyte differentiation, and inhibition of oxidative PPP or folate metabolism reduces histone acetylation. **a**, **b**, Oil Red O staining of 3T3-L1 cells transfected with control, different sets of *ME1* (**a**) or *ME2* siRNA (**b**) in the presence of increasing amounts of NADPH after 7 days of differentiation. Wells and higher magnification images are shown (left). Oil Red O staining was quantified (right). Protein expression is shown below. **c**, 3T3-L1 preadipocytes treated with or without 6-AN were induced to differentiate for 7 days. (left and middle) Differentiation-induced lipid droplet accumulation was visualized by Oil Red O staining and quantified. (right) Acid extracts were analyzed by western blot with antibodies against acetylated histones. Total H3 was used as loading control. **d**, 3T3-L1 preadipocytes transfected with control, *G6PD* or *MTHFD2* siRNA were induced to differentiate for 7 days. Cellular NADPH levels were analyzed. **e**–**g**, $NADP^+$/NADPH ratios in differentiating 3T3-L1 adipocytes (**e**) U2OS cells (**f**) and HCT116 cells (**g**) treated with control, *ME1*, *ME2*, *G6PD* or *MTHFD2* siRNA as indicated were determined respectively. The protein expression was determined by western blot. Actin was used as loading control. **h**, Expressions of acetylated histones in U2OS cells and HCT116 cells treated with control, *G6PD* or *MTHFD2* siRNA as indicated. Actin and total H3 were used as loading controls. In **a**, **b, c, d, e, f, g**, n = 3 biological replicates; Data are mean ± s.d.. Statistical significance was determined by two-tailed unpaired *t*-test. NS, not significant. In **a**,**b** (right, below panel), **c** (right panel), **e**–**g** (right panel), **h**, western blots represent three independent experiments. The samples derived from the same experiment and the blots were processed in parallel.

nature research

Corresponding author(s): Wenjing Du

Last updated by author(s): Nov 28, 2020

Reporting Summary

Nature Research wishes to improve the reproducibility of the work that we publish. This form provides structure for consistency and transparency in reporting. For further information on Nature Research policies, see Authors & Referees and the Editorial Policy Checklist.

Statistics

For all statistical analyses, confirm that the following items are present in the figure legend, table legend, main text, or Methods section.

n/a	Confirmed
☐	☒ The exact sample size (*n*) for each experimental group/condition, given as a discrete number and unit of measurement
☐	☒ A statement on whether measurements were taken from distinct samples or whether the same sample was measured repeatedly
☐	☒ The statistical test(s) used AND whether they are one- or two-sided *Only common tests should be described solely by name; describe more complex techniques in the Methods section.*
☒	☐ A description of all covariates tested
☐	☒ A description of any assumptions or corrections, such as tests of normality and adjustment for multiple comparisons
☐	☒ A full description of the statistical parameters including central tendency (e.g. means) or other basic estimates (e.g. regression coefficient) AND variation (e.g. standard deviation) or associated estimates of uncertainty (e.g. confidence intervals)
☐	☒ For null hypothesis testing, the test statistic (e.g. *F*, *t*, *r*) with confidence intervals, effect sizes, degrees of freedom and *P* value noted *Give P values as exact values whenever suitable.*
☒	☐ For Bayesian analysis, information on the choice of priors and Markov chain Monte Carlo settings
☒	☐ For hierarchical and complex designs, identification of the appropriate level for tests and full reporting of outcomes
☒	☐ Estimates of effect sizes (e.g. Cohen's *d*, Pearson's *r*), indicating how they were calculated

Our web collection on statistics for biologists contains articles on many of the points above.

Software and code

Policy information about availability of computer code

Data collection	Flexstation3(Molecular devices) was used for the absorbance measurement. All real-time PCR reactions were performed using the 7900HT Fast Real-Time PCR System(Applied biosystems). Surface plasmon resonance analysis was performed using Biacore T200 biomolecular interaction analysis system(GE Healthcare). Autodock Vina program(v1.1.2), Amber16 and Amber 18 were used to conduct molecular docking. Glucose and glutamine consumption was determined using a YSI 7100 Multiparameter Bioanalytical System(YSI).
Data analysis	All graphing and data analysis were conducted using Graphpad Prism(v8.0). Image J(v2.0.2) was used for the Western Blot band intensity measurement. In CHIP-seq analysis, BWAsoftware(v0.7.15) was used for CHIP-seq alignment. SAMtools(v1.9) and BEDtools(v2.28.0) were used to remove the nonprimary alignment or blacklisted regions from aligned data. MACS2(v2.1.1) was used for CHIP-seq peak calling. DeepTools (v3.3.0) was used to make bigWig files and plot heat maps of ChIP–seq signal. The affinity parameters in SPR were analyzed by BIAcore T200 evaluation software. Molecular docking was processed with Autodock Tools, and the docking poses were analyzed and visualized by PyMOL(v1.8). Maestro program(2018-3) was used to visualize interactions in the protein/ligand interface.

For manuscripts utilizing custom algorithms or software that are central to the research but not yet described in published literature, software must be made available to editors/reviewers. We strongly encourage code deposition in a community repository (e.g. GitHub). See the Nature Research guidelines for submitting code & software for further information.

Data

Policy information about availability of data

All manuscripts must include a data availability statement. This statement should provide the following information, where applicable:

- Accession codes, unique identifiers, or web links for publicly available datasets
- A list of figures that have associated raw data
- A description of any restrictions on data availability

The CHIP-seq data is available at: http://www.ncbi.nlm.nih.gov/geo/query/acc.cgi?acc=GSE137694. The crystal structure used in molecular docking is available with PDB ID: 5AQ1 and 4A69. Source data for western blots are provided with this paper. All other data in this study are available from the corresponding authors upon reasonable request.

Field-specific reporting

Please select the one below that is the best fit for your research. If you are not sure, read the appropriate sections before making your selection.

☒ Life sciences ☐ Behavioural & social sciences ☐ Ecological, evolutionary & environmental sciences

For a reference copy of the document with all sections, see nature.com/documents/nr-reporting-summary-flat.pdf

Life sciences study design

All studies must disclose on these points even when the disclosure is negative.

Sample size	No statistical methods were used to predetermine sample size. Sample size was based on standard protocol in the field and previous experimental observations.
Data exclusions	No date were excluded.
Replication	All the images, immunoblots and statistical graphs are representative of at least three experiments, unless otherwise stated. Experiments were performed independently. All attempts at replication were successful.
Randomization	Age and gender matched mice were randomly allocated to experimental groups. Mice used for each experiment were littermate. For cell culture experiments, individual wells were randomly assigned to treatments. Randomization does not apply to genetic analysis, since samples were genetically modified.
Blinding	Animal experiments were carried out blinded to the genotype of the mice. Besides, Blinding was not performed in other data collections and analysis, since data is quantitative in nature.

Reporting for specific materials, systems and methods

We require information from authors about some types of materials, experimental systems and methods used in many studies. Here, indicate whether each material, system or method listed is relevant to your study. If you are not sure if a list item applies to your research, read the appropriate section before selecting a response.

Materials & experimental systems

n/a	Involved in the study
☐	☒ Antibodies
☐	☒ Eukaryotic cell lines
☒	☐ Palaeontology
☐	☒ Animals and other organisms
☒	☐ Human research participants
☒	☐ Clinical data

Methods

n/a	Involved in the study
☐	☒ ChIP-seq
☒	☐ Flow cytometry
☒	☐ MRI-based neuroimaging

Antibodies

Antibodies used	Antibodies were used in according to the manufacturer's directions. Antibodies used in IB: ME1 (Abcam, Clone: polyclonal, Cat#Ab97445, Lot# GR3291218-5, 1: 1000); ME2 (Abcam, Clone: EP7217, Cat#Ab139686, Lot#GR3291064, 1: 1000); β-actin (Proteintech, Clone: 2D4H5, Cat#66009-1, Lot#10004156, 1: 3000); Ac-H2B (Millipore, Clone: polyclonal, Cat#07-373, Lot#2794875, 1: 3000); Ac-H3 (Millipore, Clone: polyclonal, Cat#06-599, Lot#3022883, 1: 3000); Ac-H4 (Active Motif, Clone: polyclonal, Cat#39243, Lot#1518001, 1: 3000); H3 (Cell Signaling Technology, Clone: polyclonal, Cat#9715, Lot#20, 1:3000); C/EBPα(Cell Signaling Technology, Clone: D56F10, Cat#8178, Lot#3, 1:500); PPARγ(Cell Signaling Technology, Clone: 81B8, Cat#2443, Lot#4, 1:500); β-tublin (Proteintech, Clone: polyclonal, Cat#10094-1-AP, 1:3000); HDAC3 (Abcam, Clone: polyclonal, Cat#Ab7030, Lot#GR210866-15, 1:3000); G6PD (Sigma-Aldrich, Clone: polyclonal, Cat#

HPA000834, 1:1000); Flag (Sigma-Aldrich, Clone:M2, Cat# F3165, 1:3000); Ncor1 (Novus, Clone: polyclonal, Cat#NB100-58824, Lot#A2, 1:500); Ncor2 (Abcam, Clone: polyclonal, Cat#Ab5802, Lot# GR3195723-5, 1:500); GST (Santa Cruz, Clone: B-14, Cat#sc-138, Lot#L2915,1:1000); HA (Cell Signaling Technology, Clone: 6E2, Cat#2999S, Lot#4,1:3000); MTHFD2 (Abcam, Clone: polyclonal, Cat#Ab151447, Lot#GR3230399, 1: 1000); FABP4 (Cell Signaling Technology, Clone: polyclonal, Cat#2120, Lot#3, 1:1000); p53 (Santa Cruz, Clone: DO-1, Cat#sc-126, Lot#A0617, 1:200); HDAC1 (Cell Signaling Technology, Clone: D5C6U, Cat#34589S, Lot#3, 1:1000); HDAC2 (Cell Signaling Technology, Clone: D6S5P, Cat#2540S, Lot#1, 1:1000); HDAC4 (Cell Signaling Technology, Clone: polyclonal, Cat#2072S, Lot#9, 1:1000); HDAC5 (Santa Cruz, Clone: B-11, Cat#sc-133106, Lot#H0916, 1:200); HDAC6 (Cell Signaling Technology, Clone: D21B10, Cat#7612S, Lot#4, 1:1000).

Validation

All the antibodies are commercially available and were validated by manufacturers. And the information can be accessed using the provided catalog numbers. Besides, some of the antibodies were also validated by knock-down or knock-out experiments.

Eukaryotic cell lines

Policy information about cell lines

Cell line source(s)

3T3-L1 preadipocytes were kindly gifted by Dr. Craig B. Thompson (Memorial Sloan Kettering Cancer Center, New York, USA). HEK293T, U2OS and HCT116 cells were purchased from ATCC (Maryland, USA). The original source of 3T3-L1 is commercial. In addition, all cell lines were cultured for no more than 2 months and their morphology was confirmed periodically to avoid crosscontamination or misuse of cell lines.

Authentication

Cell lines were authenticated by short tandem repeats (STR) profiling.

Mycoplasma contamination

Cells were tested negative for mycoplasma contamination.

Commonly misidentified lines
(See ICLAC register)

No misidentified lines were used.

Animals and other organisms

Policy information about studies involving animals; ARRIVE guidelines recommended for reporting animal research

Laboratory animals

Experiments were performed using 12 to 16 weeks old male C57Bl/6J mice, which are genetically engineered. All animals were maintained in groups 5-6 animals on a 12/12-h light/dark cycle at 22℃ with around 50% humidity, and give ad libitum access to standard food and water.

Wild animals

The study did not involve wild animals.

Field-collected samples

The study did not involve samples collected from the field.

Ethics oversight

All researches involving animals were approved by and performed in accordance with the guidelines of the Institutional Animal Care and Use Committee at Peking Union Medical College.

Note that full information on the approval of the study protocol must also be provided in the manuscript.

ChIP-seq

Data deposition

☒ Confirm that both raw and final processed data have been deposited in a public database such as GEO.

☒ Confirm that you have deposited or provided access to graph files (e.g. BED files) for the called peaks.

Data access links
May remain private before publication.

https://www.ncbi.nlm.nih.gov/geo/query/acc.cgi?acc=GSE137694

Files in database submission

H2B_siC_clean.fq.gz
H2B_siME1_clean.fq.gz
H2B_siME2_clean.fq.gz
H3_siC_clean.fq.gz
H3_siME1_clean.fq.gz
H3_siME2_clean.fq.gz
In_siC_clean.fq.gz
In_siME1_clean.fq.gz
In_siME2_clean.fq.gz
NC_H3_1_clean_1.fq.gz
NC_H3_2_clean_1.fq.gz
NC_IN_1_clean_1.fq.gz
NC_IN_2_clean_1.fq.gz
SI1_H3_1_clean_1.fq.gz
SI1_H3_2_clean_1.fq.gz

SI1_IN_1_clean_1.fq.gz
SI1_IN_2_clean_1.fq.gz
SI2_H3_1_clean_1.fq.gz
SI2_H3_2_clean_1.fq.gz
SI2_IN_1_clean_1.fq.gz
SI2_IN_2_clean_1.fq.gz

Genome browser session
(e.g. UCSC)

No applicable-visualized data using IGV.

Methodology

Replicates

No technical replicates for anti-Ac-H2B or Ac-H3 CHIP-seq; n=2 technical replicates for anti-HDAC3 CHIP-seq.

Sequencing depth

3G dates and 10M reads of every sample.

Antibodies

Acetyl-histone H3 (ac-H3, #06-599), acetyl-histone H2B (ac-H2B, #07-373) antibodies were from Millipore (Temecula, CA, USA). HDAC3 (#ab7030) were purchased from Abcam(Cambridge, MA, USA).

Peak calling parameters

All mapped reads were sorted by SAMtools with the options "-f 2 -q 10 -b -@ 20". Peak calling for ChIP-seq data was carried out by MACS2 under parameter "-g mm -p 0.005 --nomodel --extsize 189 --call-summits".

Data quality

Only the sequences with mapping quality higher than 25 were kept for further analysis.

Software

MACS2 (v2.1.1), BEDTools (v2.28.0)